

1

2                   **The Great Colorado Flood of September 2013**

3

4       David Gochis<sup>1</sup>, Russ Schumacher<sup>2</sup>, Katja Friedrich<sup>3</sup>, Nolan Doesken<sup>2</sup>, Matt Kelsch<sup>1</sup>, Juanzhen  
5       Sun<sup>1</sup>, Kyoko Ikeda<sup>1</sup>, Daniel Lindsey<sup>6</sup>, Andy Wood<sup>1</sup>, Brenda Dolan<sup>2</sup>, Sergey Matrosov<sup>3,4</sup>, Andrew  
6       Newman<sup>1</sup>, Kelly Mahoney<sup>3</sup>, Steven Rutledge<sup>2</sup>, Richard Johnson<sup>2</sup>, Paul Kucera<sup>1</sup>, Pat Kennedy<sup>2</sup>,  
7                   Daniel Sempere-Torres<sup>5</sup>, Matthias Steiner<sup>1</sup>, Rita Roberts<sup>1</sup>, Jim Wilson<sup>1</sup>, Wei Yu<sup>1</sup>, V.  
8                   Chandrasekar<sup>2</sup>, Roy Rasmussen<sup>1</sup>, Amanda Anderson<sup>1</sup>, Barbara Brown<sup>1</sup>

9

10                  Submitted to:

11                  *The Bulletin of the American Meteorological Society*

12                  Date Submitted: 7 April, 2014

13                  Revision Submitted: 12 August, 2014

14

- 15       1. National Center for Atmospheric Research  
16       2. Colorado State University  
17       3. University of Colorado  
18       4. National Oceanic and Atmospheric Administration, Earth Systems Research Laboratory  
19       5. Centre de Recerca Aplicada en Hidrometeorologia (CRAHI), Universitat Politecnica de  
20                   Catalunya, Barcelona, Spain  
21       6. NOAA Center for Satellite Applications and Research

22 Corresponding author: David J. Gochis, NCAR/UCAR, 3090 Center Green Drive, Boulder, CO

23 80301, email: gochis@ucar.edu

24     **CAPSULE**  
25     A detailed overview of the uncharacteristic meteorological conditions that caused tropical-like,  
26     widespread, heavy rainfall and catastrophic flooding across the Colorado Front Range in  
27     September 2013.

28

29     **ABSTRACT**

30     During the second week of September 2013 a seasonally-uncharacteristic weather pattern  
31     stalled over the Rocky Mountain Front Range region of northern Colorado bringing with it  
32     copious amounts of moisture from the Gulf of Mexico, Caribbean Sea and the tropical Eastern  
33     Pacific Ocean. This feed of moisture was funneled towards the east facing mountain slopes by  
34     a series of mesoscale circulation features resulting in several days of unusually widespread  
35     heavy rainfall over steep mountainous terrain. Catastrophic flooding ensued within several  
36     Front Range river systems that washed away highways, destroyed towns, isolated communities,  
37     necessitated days of airborne evacuations, and resulted in eight fatalities (NWS, 2014). The  
38     impacts from heavy rainfall and flooding were felt over a broad region of northern Colorado  
39     leading to 18 counties being designated as federal disaster areas and resulting in damages  
40     exceeding \$2B. This study explores the meteorological and hydrological ingredients that led to  
41     this extreme event. After providing a basic timeline of events, synoptic and mesoscale  
42     circulation features of the event are discussed. Particular focus is placed on documenting how  
43     circulation features, embedded within the larger synoptic flow, served to funnel moist inflow  
44     into the mountain front driving several days of sustained orographic precipitation. Operational  
45     and research networks of polarimetric radar and surface instrumentation were used to evaluate

46 the cloud structures and dominant hydrometeor characteristics. The performance of several  
47 quantitative precipitation estimates, quantitative precipitation forecasts, and hydrological  
48 forecast products are also analyzed with the intention of identifying what monitoring and  
49 prediction tools worked and where further improvements are needed.

50  
51  
52  
53  
54  
55  
56  
57  
58  
59  
60

61   **Event Synopsis**

62   During the period of 9-16 September 2013, a large area of heavy rainfall, with local amounts  
63   exceeding 450 mm, fell over a broad region of the Colorado Front Range foothills and adjacent  
64   plains (Figures 1 and 2). An event timeline shown in Figure 3 chronicles the sequence of events  
65   both leading up to and following the core periods of heavy rainfall and flooding. The most  
66   intense, widespread, and persistent rainfall along the Front Range occurred on 11-12  
67   September. While flash-flooding from locally heavy rainfall in mountain canyons is not  
68   uncommon in this region, many characteristics of the Sept. 2013 floods were exceptional.  
69   These characteristics include the protracted duration of heavy rainfall and the widespread  
70   spatial extent and prolonged duration of flooding, days to weeks following cessation of rainfall.  
71   Not only were flooding impacts felt in narrow mountain canyons, but flooding across the Front  
72   Range combined into a large-scale, multi-state flood event as tributary waters swelled and  
73   flowed down the South Platte River onto the High Plains across Northeast Colorado and into  
74   Nebraska.

75

76   The severe flooding of many regional river systems, localized flash flooding, and the landslides  
77   and debris flows that occurred claimed eight lives and produced damage, exceeding US\$2  
78   billion (Adam Smith, National Climatic Data Center, personal communication and NWS, 2014)  
79   to private and public properties in Front Range communities. Federal, state, and local  
80   emergency response entities including multiple U.S. National Guard units were activated to  
81   assist in rescue operations. Multiple communities in the region experienced massive  
82   destruction, and recovery efforts continue as of this writing. The level of destruction caused by

83 the September floods of 2013 had not been witnessed in this region for several decades.  
84 Compiling information from the Colorado Climate Center, the National Weather Service, the  
85 United States Geological Survey, as well as State and Federal disaster response agencies,  
86 Sidebar 1 lists some of the major societal impacts and Sidebar 2 details many of the  
87 documented rainfall records that were set. As with any large natural disaster, these statistics  
88 form only a thin wrapper on the physical and emotional costs incurred to individuals and  
89 communities that have had to live through such events.

90

91 This study documents the climatological, meteorological, and surface hydrological processes  
92 responsible for producing such widespread destruction. The multi-day event is examined from  
93 the perspective of the causative mechanisms for heavy rainfall and associated hydrologic  
94 responses. We explore the event in terms of large-scale moisture transport patterns, the  
95 mesoscale features that localized heavy rainfall, and the storm- and cloud-scale processes that  
96 were observed by a comparatively rich and technologically-advanced observational network,  
97 though many of those observations were not available in real-time. In addition, this article  
98 recounts the event in the context of operational quantitative precipitation estimates (QPE),  
99 quantitative precipitation forecasts (QPF), and operational flood forecasts. While the system  
100 that produced heavy rainfall occurred over a one-week period (9-16 September) and covered a  
101 large, multi-state area, this article primarily focuses on the period of 11-13 September in  
102 Boulder and Larimer Counties of Colorado's northern Front Range, arguably the area most  
103 severely impacted by the September floods. It is important to note that several other areas of  
104 intense rainfall and flooding took place simultaneously in regions east and south of the

105 northern Colorado Front Range, and also in parts of New Mexico and southern Wyoming. A  
106 complete description including these other areas is beyond the scope of this study.

107

108 The hydrometeorological processes described herein are organized according to space and time  
109 scales over which those processes operated ranging from the large-continental, synoptic-  
110 climatic setting down to the scale of small watersheds. The “large-scale” circulation setting (i.e.  
111 1000’s of km) in the period leading up to and during the flood event is described along with a  
112 chronology of heavy precipitation episodes along with a more “regional”, or mesoscale (i.e., 10-  
113 100s of km), description of atmospheric features that played important roles in localizing the  
114 regional rainfall patterns and contributed to episodes of particularly intense rainfall. Findings  
115 from a focused analysis of “cloud-scale” processes of several different cloud and precipitation  
116 observational platforms that were operating during the event are then given. A chronology of  
117 the flooding generated by the heavy rainfall follows along with a summary discussion of runoff  
118 generation processes that played significant roles in translating rainfall into streamflow. A  
119 brief analyses of several of the operational quantitative precipitation estimates (QPE) is then  
120 provided followed by a short summary of several quantitative precipitation forecast (QPF)  
121 products and National Weather Service (NWS) operational streamflow predictions. We  
122 conclude with a summary of lessons learned from this event so far and enumerate some of the  
123 opportunities for incorporating these findings into future hydrometeorological prediction  
124 systems. Lastly, while there is much to be learned from the shared experiences of people and  
125 institutions in coping with such natural disasters, this is outside the scope of this work.

126 Therefore, we only attempt to provide a high-level, comprehensive overview of the  
127 hydrometeorological processes occurring during the September 2013 flooding event.

128

129 **The Synoptic Setting**

130 The large-scale atmospheric pattern that supported persistent heavy rainfall in northern  
131 Colorado during 10-16 September 2013 consisted of a blocking ridge over the Canadian Rockies  
132 and a slow-moving, cutoff, upper-level cyclonic circulation to its south over the western U.S.  
133 (Fig. 4a and b). The blocking anticyclone assisted in keeping the western-U.S. cutoff circulation  
134 in place for several days, and to the east and southeast of this circulation, moist air was  
135 transported northward and westward toward the Front Range in Colorado (Figs. 4b, c and d).  
136 The 500-hPa pattern bears some similarity to the Maddox et al. (1980) “Type I” western flash-  
137 flood pattern (their Fig. 1), with a strong ridge over western North America, although Maddox  
138 et al.’s pattern showed the heavy rainfall occurring near a shortwave trough moving northward  
139 on the west side of the ridge rather than ahead of a cutoff circulation underneath the ridge.

140

141 The week preceding the flood event (2-8 September) was marked by a stretch of extreme heat  
142 in the Colorado Front Range region where three daily high-temperature records were tied or  
143 broken in Denver (NWS 2013b). This heat wave was associated with a large blocking ridge  
144 across western North America (Fig. 4a). Northward flow along the western periphery of the  
145 North American sub-tropical anticyclone, situated over the southeast U.S. (Fig. 4a), intensified  
146 on 10-11 September and, in concert with the stagnating cutoff low to the west, began to

147 support deep southerly flow into the High Plains, as well as easterly (upslope) low-level flow  
148 into the Colorado Front Range (Fig. 4d). Furthermore, a long east-west surface baroclinic zone  
149 extended from eastern Canada westward into Colorado (see broad swath of east-west oriented  
150 clouds in Fig. 4b) with an associated surface front, served, in addition to orographic lift, as a  
151 persistent low-level focusing mechanism for ascent along the Front Range during 11-13  
152 September.

153

154 This large-scale atmospheric flow pattern brought highly anomalous moisture to northern  
155 Colorado for an extended period of time during 9-16 September (Fig. 4c). The moisture source  
156 for this transport appears to have been fed by broader-scale anomalous oceanic conditions in  
157 the western hemisphere tropical oceans where positive sea surface temperature (SST)  
158 anomalies from 1-3° C were observed (Appendix 1). Standardized anomalies (e.g., Hart and  
159 Grumm 2001) of precipitable water (PW) were 2-4 standard deviations above normal in a  
160 corridor extending from the Gulf of Mexico and the tropical eastern Pacific into the  
161 intermountain west near and ahead of the cutoff circulation (Fig. 4c). The Denver radiosonde  
162 observation set new daily records for PW for six consecutive 12-hourly soundings (Fig. 5a), with  
163 PW exceeding 25 mm in nearly all soundings during 10-16 September, a high value for this  
164 climatologically dry region and season. On 12 September, the easterly winds at 700 hPa (Figs.  
165 5b and 4d) were greater than 3 standard deviations away from the mean in northern Colorado  
166 with anomalous easterlies in place from 8-16 September.

167

168 The atmospheric sounding from Denver in Figure 5b indicates that lower atmospheric stability  
169 during this period of near saturated conditions was largely moist adiabatic and neutral with  
170 only modest amounts of convective available potential energy (CAPE) present (see indices in  
171 Fig. 5b). Although this sounding passed through cloud and precipitation on ascent and thus is  
172 not representative of cloud-free conditions, it is generally similar in structure to other Denver  
173 soundings during this week. Furthermore, the presence of only modest CAPE is consistent with  
174 the Storm Prediction Center's real-time mesoanalysis over much of eastern Colorado (not  
175 shown). Comparing this sounding to the mean 1200 UTC September temperature and  
176 dewpoint soundings reveals that the dewpoint is considerably greater than one standard  
177 deviation above the September mean from the surface to 400 hPa. There was a very high  
178 freezing level (approx. 600 hPa or 4200 m), such that precipitation took the form of rain all the  
179 way to the highest levels of the terrain. Finally, there was a prominent isothermal layer at 0 deg  
180 C, indicating an important role of ice processes in precipitation formation although  
181 considerable warm rain below this level likely also occurred.

182

### 183 **The evolution of rainfall between 11-15 Sep 2013**

184 As tropical moisture moved into the region on 10-11 September, temperatures remained in the  
185 16-18°C range (low 60s °F) and widely scattered storms ensued. Repeated periods of heavy  
186 rainfall (i.e. rain rates around  $25 \text{ mm h}^{-1}$  or greater) and flooding began in the evening (local  
187 time) on the 11th with the heaviest rains focusing on the Front Range (see Fig. 1 for a map of  
188 the local geography). Local, sustained rates between  $25\text{-}50 \text{ mm h}^{-1}$  ( $1\text{-}2 \text{ inches h}^{-1}$ ) occurred  
189 near Boulder spreading northwest into the mountains towards Estes Park, CO. Heavy rainfall in

190 and along the mountain front accumulated overnight resulting in total amounts exceeding 200  
191 mm (8 inches) in many locations and amounts over 50 mm (2 inches) extending all the way up  
192 to the Continental Divide. Persistent rainfall continued through 12 September becoming  
193 intense again in the afternoon, increasing rainfall totals in the heaviest hit areas to over 380  
194 mm (15 inches).

195

196 Heavy rains diminished to widespread drizzle and intermittent showers during the day on 13  
197 September. Clearing weather on 14 September allowed air support and emergency rescue  
198 efforts for approximately 24 hours (see timeline in Fig. 3 and list of event impacts in Sidebar 2).

199 Heavy rains, some associated with deep convection, returned on Saturday afternoon (14<sup>th</sup>),  
200 primarily on the plains east of Interstate 25 with flooding occurring northeast of the cities of  
201 Denver and Aurora. One last surge of moisture with widespread 25-50 mm (1-2 inches) rains  
202 occurred across the entire Front Range during the day on 15 September. Rainfall rates during  
203 this final episode were moderate but widespread and occurred on saturated soils so that runoff  
204 production was very high.

205

206 Figure 6 shows a time-longitude evolution of the rainfall event as depicted by radar reflectivity  
207 from the Denver (KFTG) Weather Surveillance Radar-1988 Doppler (WSR-88D) from 9-13  
208 September. Two distinct rainfall regimes are observed; one in which radar echoes show a west-  
209 to-east (lower left to upper right track) movement (00 UTC 9 September through 00 UTC 11  
210 September), and a second regime where radar echoes are either stationary or have an east-to-

211 west (lower right to upper left track), or “upslope”, movement (00 UTC 11 Sep- through 00 UTC  
212 13 Sep). Figure 6b highlights this second quasi-stationary and upslope regime, and reveals the  
213 presence of persistent, stationary and/or regenerating radar echoes over the mountains for  
214 nearly 48 hours (the region within the dotted inset box in Fig. 6b). These radar echoes  
215 approach 40 dBZ just after 00 UTC on 12 Sep. and again around 00 UTC on 13 Sep. Farther east,  
216 many echoes during this period are seen moving towards the mountains. This period of  
217 persistent heavy rainfall along the mountains within the dotted box was the predominant  
218 source of rain associated with most of the catastrophic flooding that occurred in Boulder and  
219 Larimer counties.

220

221 The spatial pattern of storm total rainfall shown in Fig. 2 reveals a complex structure. Although  
222 orographic lifting was a key process contributing to heavy rainfall, the southeast-to-northwest  
223 swath of heaviest rainfall (see Fig. 2) was not directly aligned with the regional north-south  
224 orographic slope. The mesoscale circulation features contributing to this complex evolution  
225 and pattern of rainfall are discussed in the following section. The most extreme rainfall  
226 amounts (totals in excess of 400 mm; 16 inches) were measured within the city limits of  
227 Boulder and in the foothills to the west and northwest. The area of heaviest rainfall extended  
228 northwestward into the St. Vrain, Little Thompson and the southern half of the Big Thompson  
229 watersheds. Rainfall in excess of 250 mm (10 inches) for the week was measured at elevations  
230 as high as 3,300 m (10,000 ft) and as far west as Estes Park. A more detailed description of the  
231 precipitation records set during the September flood event is provided in Sidebar 2.

232

233 **Mesoscale circulation features**

234 While synoptic-scale features conditioned the environment for a persistent wet period over a  
235 broad region from southern Wyoming through central New Mexico, there were many  
236 mesoscale processes responsible for localizing heavy rainfall along the mountain front regions  
237 of Colorado and for the episodes of especially heavy rainfall that exacerbated flooding  
238 responses in Boulder and Larimer Counties. Fine-scale wind analyses were generated from the  
239 VDRAS (Variational Doppler Radar Analysis System, Sun and Crook 1997) for the main heavy  
240 rain episodes on 11-12 September (Figure 7). Observations used by the VDRAS 4DVar (four-  
241 Dimensional Variational) data assimilation system include radar radial velocity and reflectivity  
242 from NWS radars located in Denver, CO (KFTG) and Cheyenne, WY (KCYS) and surface data from  
243 surface meteorological stations in the Rocky Mountain Front Range region. A movie loop of the  
244 VDRAS analyzed convergence, horizontal wind at 0.15 km above ground level (AGL), and  
245 observed radar reflectivity for the period between 1800 UTC, 11 and 0800 UTC, 12 September is  
246 provided in Electronic Supplement A. The VDRAS analyses revealed a cyclonic mesoscale  
247 circulation in the southern part of the domain that gradually intensified from approximately  
248 1800 UTC to 2300 UTC 11 September. This circulation persisted, remaining relatively  
249 stationary, until around 0600 UTC on 12 September and was associated with enhanced east-  
250 southeasterly flow in the region over Denver and Boulder. Although this circulation developed  
251 in the same general region as the “Denver cyclone” previously documented in the literature  
252 (e.g., Szoke et al. 1984; Wilczak and Christian 1990; Crook et al. 1990), ongoing research aims to  
253 determine whether the processes are similar. Strong convergence along with enhanced

254 southeasterly winds (Electronic Supplement A) were present on the north side of the  
255 circulation, and a band of relatively deep convection developed within this region of enhanced  
256 upslope flow (Fig. 7). Observed reflectivity from a mosaic of KFTG (Denver) and KCYS  
257 (Cheyenne) WSR-88D radar echoes in excess of 30 dBZ initiated near the center of this updraft  
258 region and then moved northwestward and also showed rotational signatures in between  
259 Denver and Boulder. The most intense and deepest convection (45 dBZ echo) occurred in  
260 Boulder County around 0600 UTC.

261

262 A second area of increased low-level convergence north of Fort Collins developed around 0200  
263 UTC (Fig. 7 and Electronic Supplement A). Around 0400 UTC, the two convective regions in  
264 Boulder and Larimer Counties appeared to converge and this merged region of heavy rain  
265 expanded northwestward from Boulder into the higher terrain near the town of Estes Park and  
266 northward along the mountain front. The period of 0400-0700 UTC was associated with peak  
267 hourly rainfall rates in excess of  $45 \text{ mm h}^{-1}$  observed from gauge data in the city of Boulder  
268 (Figure 8). As discussed in the next section, this episode represented one of the few periods of  
269 vigorous, electrified, deep convection during the September 2013 rainfall event.

270

## 271 **Cloud and hydrometeor processes**

272 Much of the precipitation during the September 2013 Colorado Flood was characterized by  
273 orographically-lifted, stratiform precipitation with some embedded convection. During most  
274 of the event, a well-defined melting layer was present and appreciable collision-coalescence

occurred between the melting layer and cloud base. Evidence for this comes from multiple observation platforms including a vertically-pointing, Ka-band, micro rain radar (MRR) located at Boulder, the NWS Denver NEXRAD radar (KFTG) and the CSU-CHILL dual-polarization Doppler radar located at Greeley (Figure 9; also see Fig. 1 for locations of these instruments). As radar analysis indicates, stratiform precipitation was produced by ice particles falling through the melting layer, melting to form raindrops which continued to grow by collision-coalescence as they fell through a 2.5-km deep warm-cloud zone (Figs. 9 and 10). Deep, saturated zones creating favorable conditions for collision-coalescence processes are uncommon in such high elevation, mid-latitude, continental interior regions. Also, unlike most rain events along the Front Range occurring in September, the cloud bases during the highest precipitation periods were very low ( $\sim$  200 m AGL based on ceilometer observations shown in Fig. 10b). CSU-CHILL radar observations collected from 12 September 1500 UTC through 13 September 0400 UTC indicated a mean increase in reflectivity below the melting layer of about 1 dBZ per km towards the surface (Fig. 9). Differential reflectivity, the ratio between horizontal and vertical polarization reflectivity signals, from the CSU-CHILL radar increased by approximately 0.2 dB per km towards the surface during the same period, further supporting the assertion that cloud droplets slowly grow to small raindrops as they fall to the surface. Even though for the period shown in Fig. 9 there is a general small increase in reflectivity ( $Z$ ) and differential reflectivity ( $Z_{dr}$ ) towards the ground indicating drop growth, mean  $Z_{dr}$  values (and hence drop sizes) are still on average smaller than usual for Front Range warm season rains (see Figure Sidebar 3b) and below the thresholds for quantitative precipitation analysis in the polarimetric retrieval algorithm used here (> 0.5 dB for  $Z_{dr}$ ; Cifelli et al. 2011).

297

298 During the period of relatively deep convection in Boulder County from 0000-0600 UTC on 12  
299 September occasional lightning was observed by the Northeast Colorado Lightning Mapping  
300 Array (LMA; Fig. 8). In addition, KFTG hydrometeor classification indicates low-density graupel  
301 close to the melting layer (see Appendix 2 for vertical profiles of hydrometeor classifications  
302 from the CSU-CHILL and KFTG radars) and the GOES-13 infrared data, also plotted in Fig. 8,  
303 showed a deep convective signal with minimum brightness temperature of -51 °C during that  
304 time. Outside of this time period, evidence of deep convection was generally lacking. Infra-red  
305 satellite imagery showed periods of shallower convection (cloud tops warmer than -40 °C)  
306 during the afternoon hours of 12 September. Some of the shallow convection appeared to  
307 produce intense warm rain showers without a well-defined bright band (Fig. 9 at a distance of  
308 75-80 km range from the CHILL radar). For most of the time period, radar estimated cloud-top  
309 heights ranged between 8-13 km MSL.

310

311 Particularly intense periods of precipitation in Boulder and Larimer Counties occurred in bands  
312 of high rainfall rates during two distinct episodes; the aforementioned 0000-0600 UTC period  
313 and a second period between 2200 UTC 12 September and 0300 UTC 13 September. During  
314 these periods, peak rainfall rates of up to  $50\text{--}70 \text{ mm h}^{-1}$  and  $40\text{--}60 \text{ mm h}^{-1}$ , respectively, were  
315 observed from multiple surface rain gauge stations (Figs. 8 and 10). Rainfall observed by quality  
316 controlled PARticle SIZe and VELOCITY (PARSIVEL-Ott, Inc.) optical disdrometers was much higher  
317 in Boulder (1665 m MSL) and Marshall (1742 m, 5 km south of Boulder) compared to two

318 PARSIVEL instruments located 12 km farther to the west in the foothills at Sugarloaf (2431 m  
319 MSL) and Melvina Hill (2225 m MSL). The two intense episodes on 12 September were  
320 characterized by smaller reflectivity values, which rarely exceeded 45 dBZ, were consistent with  
321 the relatively small raindrop sizes observed, with mean diameters ranging mainly between 1-  
322 1.8 mm (Fig. 10c). The reflectivity-rainfall ( $Z-R$ ;  $Z$  in  $\text{mm}^6 \text{ m}^{-3}$ ) relationship derived from the  
323 disdrometer observations (Fig. Sidebar 3; Boulder  $132R^{1.3}$ ; Marshall  $106R^{1.3}$ ; Melvina Hill  
324  $120R^{1.5}$ ; Sugarloaf  $149R^{1.4}$ ) indicates that the rainfall did not show typical characteristics of mid-  
325 latitude rain, but instead showed strongly tropical rainfall characteristics, a feature also  
326 observed during the Fort Collins flash flood in 1997 (Petersen et al. 1999). A more detailed  
327 characterization of hydrometeors observed during the event and their impact on polarimetric  
328 radar data is provided in Sidebar 3.

329

### 330 **Hydrologic processes and impacts**

331 Rainfall-induced flooding in the Rocky Mountain region of the United States has been well  
332 documented (e.g. Michaud 2001), including extreme events such as the Rapid City flash flood of  
333 June 1972 that resulted in 220 fatalities, the Big Thompson flash flood of July 1976 (Caracena et  
334 al. 1979; Maddox et al. 1978) that resulted in 144 fatalities, and the Fort Collins flash flood of  
335 July 1997 (Petersen et al. 1999) that resulted in 5 fatalities and \$200 million dollars in damage.  
336 Long-term historical data show an event similar to September 2013 took place in the same  
337 region in September 1938 though there is little information available on the  
338 hydrometeorological details surrounding that event (BASIN, 2014).

339

340 A key challenge in providing confident estimates of peak flows during many flood events is the  
341 fact that streamflow gauges along the most heavily flooded river systems were destroyed or  
342 experienced river stages that exceeded established river stage-streamflow relationships (i.e.  
343 “rating curves” – see NWS, 2014 for additional information on the issue of rating curves during  
344 the Sept. 2013 flood event). Since the flood event several reports have been released that  
345 have attempted to summarize, by means of post-flood peak flow reconstruction methods or re-  
346 calibrated rating curves, peak flow conditions during the flood along with estimates of the  
347 statistical probability, or recurrence intervals (e.g. Yochum and Moore 2013; Stewart 2013,  
348 Houck 2014; NWS 2014). An abbreviated synthesis of these peak flow values is provided in  
349 Table 1 and locations of peak flow values for a host of river systems are also shown in Figure 1.  
350 Because peak flow values on any given river system are controlled to a large degree by the total  
351 contributing area of a river’s watershed, peak flow values are often normalized by watershed  
352 area, to facilitate intercomparison of peak flows between watersheds (i.e. “unit discharges”)  
353 and thus, unit discharge values are also provided in Table 1. It is important to note that there  
354 are considerable uncertainties in peak flow and return flow estimates due to the dynamic  
355 nature of flooding events themselves, debris suspended in the flow, rapidly changing channel  
356 geometries, assumptions involved in flow velocity conditions during the flood and the statistical  
357 uncertainty inherent in characterizing extreme or rare events.

358

359 From south to north the worst-affected systems were Fourmile Canyon in the Boulder Creek  
360 watershed, James Creek and Lefthand Creek within and downstream of Jamestown, both the

361 south and north branches of the St. Vrain River feeding into Lyons, the Little Thompson River,  
362 Fish Creek, the upper Big Thompson River and Fall Creek near Estes Park, the North Fork and  
363 mainstem of the Big Thompson River, Buckhorn Creek and portions of the Cache la Poudre  
364 River (See Fig. 1 for map of principal watersheds). Regions impacted by recent wildland fires  
365 (see Fig. 1 for map of recent burn areas) tended to exhibit particularly high unit-discharge  
366 values (e.g., the Skin Gulch drainage in the Poudre River watershed, Buckhorn Creek in the Big  
367 Thompson watershed and Fourmile Creek in the Boulder Creek watershed). The reasons for  
368 such extreme hydrologic responses in burn areas are manifold including removal of vegetation  
369 that intercepts rainfall, reduction in surface ponding or “storage” capacity, a reduction in  
370 surface roughness to overland flow, and potential reductions in soil infiltration capacity caused  
371 by soil chemical and physical responses to extreme heat during the fires (see Moody et al. 2013  
372 for a review on fire-hydrology interactions).

373

374 As flood waves propagated out onto the plains, several communities there suffered massive  
375 damage. The worst-affected river systems on the Colorado plains were the St. Vrain River  
376 through Longmont, the Big Thompson River through Loveland, Westerly Creek and Sand Creek,  
377 north of Denver and the South Platte River through the towns of Kersey, Milliken and Evans (all  
378 near Greely Colorado on Fig. 1). Local flooding was widespread throughout several small urban  
379 channel systems and many rural, agricultural properties and communities were hard hit by  
380 flooding on the plains (Stewart 2013; NWS 2014).

381

382 Infrastructure to manage water resources and floodwaters throughout the region has largely  
383 girded the region from recent widespread flooding impacts. The events of September 2013  
384 exposed several vulnerabilities in regional flood-protection infrastructure, but a large number  
385 of flood control structures did perform according to their design and likely prevented additional  
386 losses in lives and property (Stewart, 2013). Table 1 provides the most recent estimates on the  
387 long-term event probabilities or “return periods” available for this event that have been  
388 compiled from various sources. On the mainstem and North Forks of the Big Thompson River  
389 the flood has been estimated to have a return period around 500 years (i.e. 1/500 or 0.2%  
390 probability), as did parts of the lower St Vrain River near Lyons, Colorado (Houck, 2014). On  
391 Boulder Creek the estimate of a 50-year flood was less exceptional, owing to the fact that the  
392 heaviest rain fell in the lower and flatter portions of the drainage where runoff production was  
393 not as efficient nor rapid.

394

### 395 **Runoff generation mechanisms**

396 While the spatial distribution and intensity patterns of rainfall played the dominant role in  
397 dictating the timing and severity of flooding in specific drainages, evolution of runoff and  
398 flooding was also influenced by land-surface characteristics, both natural and human-  
399 engineered. Many flood-affected regions of the 2013 Colorado floods are characterized by  
400 large variations in slope, soil types, soil thickness, land use, and forest cover. Several of the  
401 most severely impacted drainages of the Colorado Front Range were those that received the  
402 heaviest rainfall in mountainous portions of their drainage areas (e.g., Fourmile Creek, Lefthand  
403 Creek, St. Vrain River, Big and Little Thompson Rivers). As the flooding from the mountain-

404 front channel systems spilled onto the plains and merged into the mainstem of the South Platte  
405 River, several communities along its path were inundated for several days after rainfall had  
406 ceased. Rising groundwater levels from perched, unconfined aquifers throughout the Front  
407 Range also created domestic flooding hazards as water percolated into basements of buildings  
408 suggesting that many regional soils became saturated. In total, the time it took from the start  
409 of severe flooding to occur in the tributary drainages until the flood wave was attenuated to  
410 below-floodstage levels on the South Platte River in western Nebraska was approximately 2  
411 weeks (as indicated by USGS streamflow observations for the South Platte River at Roscoe,  
412 Nebraska). As such, the September floods of 2013 transcended several timescales of flooding  
413 from short-term “flash floods” on the order of tens of minutes all the way out to “slow-rise”  
414 floods on the order of days to weeks. This timescale transcendence of severe flooding impacts  
415 was one of the unique characteristics of this event.

416

417 The range in flooding responses suggests that multiple flood-generation mechanisms were  
418 operating during this prolonged event. There were likely numerous areas of “infiltration  
419 excess” (i.e., where rainfall rates exceed soil infiltration rates) runoff mechanisms operating  
420 during some of the heavy rainfall that occurred the night of 11-12 September (Yochum and  
421 Moore, 2013; Coe et al., 2014; NWS, 2014). Fast runoff responses to heavy rain was  
422 widespread in steep canyon areas with little or no soil cover as well as in recently burned areas.  
423 However, as rainfall persisted, and as evidenced by the aforementioned groundwater impacts  
424 and by *in-situ* soil moisture measurements (see soil moisture measurements from the U. of  
425 Colorado Mountain Research Station in Appendix 3), soils appeared to approach saturated

426 conditions from the plains all the way up to 3300 m (10,000 ft) above MSL. Under such  
427 saturated soil conditions there is an increased likelihood of “saturation excess” runoff  
428 generation mechanisms (i.e., where nearly-saturated soils have very little capacity to absorb  
429 more water). Additionally, across most of the Front Range river system, streamflow recession  
430 (i.e. the time it takes for streamflow to return to more normal seasonal values) lasted for  
431 months after the September event. The late-autumn/early-winter period is usually a time  
432 when many Front Range river systems are at their lowest flow levels or run dry. However,  
433 many of these systems carried appreciable flow into January 2014 (not shown) compared with  
434 more typical seasonal flow values which potentially have a cross-seasonal impact on  
435 streamflow production during snowmelt in the following spring.

436

#### 437 **Analysis of Quantitative Precipitation Estimate (QPE) products**

438 The backdrop of steep, complex topography along with the predominance of low altitude cloud  
439 bases with high concentrations of small-to-medium, nearly-spherical rain drop sizes presented  
440 a major challenge for operational QPE products which resulted in significant uncertainty as to  
441 how much rain was falling and where. Figure 11 shows the 2-day total rainfall from five  
442 different QPE products derived from Level II NWS-NEXRAD radar data at surface rain gauge  
443 sites, and illustrates the large uncertainties that existed among the QPE products. These  
444 products include three “radar-only” products where the difference between the products was  
445 selection of the radar reflectivity rainfall (Z-R) relationship (KFTG “Default” or “Tropical”) or the  
446 use of multi-parameter polarimetric radar information (KFTG “Dual-pol”). The default regional  
447 Z-R relationship for the Denver NEXRAD radar (KFTG) is  $Z=300R^{1.4}$ . An aggressive ‘tropical’

448 rainfall Z-R relationship of  $Z=32R^{1.65}$  (J. Wilson, personal communication) was also used for  
449 comparison. The polarimetric radar QPE product is developed by the NWS after Ryzkov et al  
450 (2005). The other two rainfall products shown are two gauge-corrected products produced by  
451 NOAA entitled the Multi-sensor Precipitation Estimate (MPE, Kitzmiller et al. 2013) and NCEP  
452 Stage-IV (Lin and Mitchell 2005). The two gauge-corrected products differ by both the number  
453 of stations used in the analysis and their quality control and bias correction procedures. With  
454 respect to the application or use of these products it is important to note that the radar-only  
455 QPE products are available in real-time minutes after the radar completes its scan while the  
456 gauge-corrected products have latencies on the order of 1-2 days. The QPE values at rain gauge  
457 sites were determined by mapping the five QPE products over a common grid space (1 km  
458 horizontal grid spacing) and then taking an inverse-distant weighted average of grid cell values  
459 from a 3 km x 3 km area centered on the nearest grid point from each gauge site using the  
460 Model Evaluation Tools software (MET-2014).

461

462 Bias maps shown in Fig. 12 and a summary table of QPE biases (Appendix Table 1), separated by  
463 three sub-regions shown as inset boxes R1, R2 and R3 on Figs. 11 and 12, highlight large  
464 discrepancies between these products, particularly in sub-region 2, but also in other areas. It is  
465 clear that the default regional NEXRAD Z-R relationship is not capable of producing realistic  
466 rainfall from this event and underestimated regional rainfall amounts by greater than 50%.  
467 Due to the dominance of small size raindrops which produce little change in the dual-  
468 polarization radar parameters as shown in the Cloud and Hydrometeor section, dual-  
469 polarization precipitation estimates, while usually better than the default NEXRAD Z-R estimate,

470 also did not verify well with regional quality-controlled gauge data. Effectively, dual-polarization  
471 estimators did not have enough differential signal to properly constrain the rainfall estimates  
472 and, as such, algorithms like the Cifelli et al. (2011) retrieval methodology used in CHILL or  
473 the Ryzkov et al. (2005) used in the NWS dual-pol retrieval still suffered some apparent  
474 deficiencies. Conversely, estimating rainfall with the aggressive tropical Z-R relationship  
475 provided much greater real-time precipitation estimates where biases were positive and on the  
476 order of 10-20%.

477

478 There was a surprising difference between the MPE and Stage-IV gauge-corrected products  
479 where the MPE product clearly exhibited superior performance. This is surprising because the  
480 products are derived from the same operational radar product and are adjusted with much,  
481 though not all, of the same gauge data. The difference between MPE and Stage IV is attributed  
482 to merging additional rain gauge data and performing additional manual quality control after  
483 more gauge data become available in the MPE product. It is evident that operational QPE  
484 products exhibited a wide range in their estimates which produced additional uncertainty for  
485 hydrometeorological forecasters and, subsequently, in decision makers who needed to respond  
486 and plan for critical operations during the event. The QPE analysis provided here and the  
487 hydrometeor descriptions presented earlier suggests there is some potential for additional  
488 value to be added to operational radar QPE products through the incorporation of additional  
489 information sources such as real-time direct measurement of precipitation amounts through  
490 gauges and, potentially, drop-size distributions and real-time Z-R relationship analyses from  
491 disdrometers, and information on microphysical processes from vertically-profiling radars.

492

493 **Analysis of Quantitative Precipitation Forecasts and Streamflow Forecasts**

494 Following the floods, the performance of operational precipitation and flood forecast products  
495 became a matter of considerable interest. In-depth information on weather forecast model  
496 skill for this event is available in NWS (2014), Schwarz (2014), Hamill (2014) and Lavers and  
497 Villarini (2013). Thus, only a brief analysis of precipitation and flood forecasts is provided here.

498

499 We present a sequence of 12-60 hour forecasts centered on the heaviest rainfall period (0000  
500 UTC 11 September – 1300 UTC 12 September), highlighting lead times relevant to the issuance  
501 of NWS watches and warnings. Figure 13 shows six predictions from operational numerical  
502 weather prediction (NWP) models (a-f), from the NCEP Weather Prediction Center (WPC)  
503 forecasters (g) and a verifying analysis (h). These forecast products are generally available  
504 during real-time to inform the official NWS WFO forecasts and consequent guidance. The QPFs  
505 show heavy precipitation was forecasted for the 60-hour period beginning 0000 UTC 11  
506 September, with all models indicating rainfall maxima exceeding 50 mm (2 inches) over this  
507 time period. (For reference, the entire monthly average precipitation for September at  
508 Boulder, Colorado is approximately 40 mm.) Most models placed a relative QPF maximum in or  
509 near the northern Front Range, though none successfully captured the large observed  
510 magnitude nor the extent of the elongated axis of heavy rainfall stretching from the Colorado-  
511 Wyoming border southward to central Colorado (Fig. 13h). The 60-hour synthesis forecast  
512 generated by human forecasters at the WPC in Fig. 13g improved upon all of the numerical

513 model forecasts in its placement, extent, and intensity of the northern Front Range QPF  
514 maximum, but still under-predicted observed totals from NCEP Stage IV by more than 50%.  
515 The two ensemble mean forecasts (Figs. 13d and f) and WPC forecast (a subjective ensemble  
516 consensus) had slightly reduced intensities and spatial granularity relative to the other  
517 forecasts, but focused the precipitation in a reasonably consistent pattern across most of the  
518 northern Front Range. The notable performance of the NWS SREF product evident in Figure.  
519 13d was also noted in the NWS Service Assessment (NWS 2014).

520

521 While the placement of precipitation maxima in the northern Front Range by most models  
522 likely offered valuable forecast guidance, spurious QPF maxima (e.g., the GFS large QPF  
523 maximum in eastern Kansas; Fig. 13a) could undercut the perception of model performance by  
524 way of false-alarm errors. The similarity of QPF from the higher resolution NAM 4-km nest (Fig.  
525 13c) to its lower-resolution parent (NAM, in Fig. 13b), suggests that increased model resolution  
526 did not substantially improve that model's forecast accuracy for the event.

527

528 In summary, operational rainfall forecasts did predict a significant precipitation event focused  
529 in the northern Front Range of Colorado, although predicted rainfall totals were far lower than  
530 what was observed. In the 1 – 2 days preceding the heaviest rainfall, the forecast guidance  
531 likely offered value to local WFO forecasters and this guidance is noted in NWS (2014).

532

533 The NWS Service Assessment (NWS 2014) also suggests that there were shortcomings in how  
534 QPF and QPE information is translated into flood guidance information and products. Two  
535 kinds of quantitative flood forecast information are typically available during events like the  
536 Colorado Front Range flood. The first is called Flash Flood Guidance (FFG) which is a time-  
537 varying, rainfall accumulation threshold above which flash flooding is likely (Clark et al., 2014).  
538 Using a combination of a soil moisture accounting model and historical rainfall and streamflow  
539 data, FFG numbers track patterns of antecedent accumulated rainfall to account for the  
540 remaining amount of water storage the land surface can provide before flooding ensues. As a  
541 result of the increasing soil saturation levels described above, FFG values from the Missouri  
542 River Basin River Forecast Center (MBRFC) decreased from over 76.2 mm (3 inches) on 9  
543 September to under 6.4 mm (0.25 inches) by 13 September for appreciable parts of Boulder,  
544 Larimer and Jefferson Counties in the Front Range region (Appendix 4). The mountainous  
545 regions of the Boulder Creek, Lefthand Creek, St. Vrain, and Little and Big Thompson  
546 watersheds saw the largest changes in FFG values during the event. These dramatic reductions  
547 in FFG values during the event aided in the dissemination of over 70 flash flood warnings issued  
548 by the Denver/Boulder and Pueblo NWS Forecast Offices during the event (NWS, 2014).

549

550 The second type of quantitative flood forecast information is point forecasts of river stage and  
551 streamflow at predetermined gauging stations. From the city of Denver north to the Wyoming  
552 border there were approximately 19 stations at which the MBRFC produced streamflow  
553 forecasts, mostly on the plains. The performance of streamflow forecasts was strongly  
554 dependent on the size and response time of the contributing catchment. In general, forecasts

555 in smaller, fast responding watersheds gave the least lead time in predicting flood stage, and  
556 showed the largest relative under-predictions. In contrast, forecasts for larger, slow-  
557 responding drainage areas were better able to predict the magnitude of river rises, despite also  
558 generally under-estimating the crest arrival time. Figure 14 illustrates these tendencies by  
559 showing sequences of river stage forecasts and observations during the event for a fast (North  
560 Fork of the Big Thompson River above Drake), medium (South Platte River at Weldona) and  
561 slow (South Platte River at Julesburg, near the Nebraska state line) response-time watersheds  
562 (with drainage areas of 305, 13,190 and 22,821 mi<sup>2</sup>, respectively). Forecasting floods in small  
563 watersheds is particularly challenging due to uncertainties in both the location and intensity of  
564 forecasted rainfall, a problem that is relatively dampened over larger forecast areas. Finally, for  
565 the larger basins analyzed, forecasts of river recession characteristics were more accurate than  
566 predictions of the rising limb of the flood hydrograph. Additional information on the  
567 verification of flood and flash flood warnings is available in NWS (2014).

568

## 569 **Conclusions**

570 The historical record of floods in the Colorado Front Range is replete with events generated by  
571 large summer thunderstorms or sustained periods of springtime rains on top of rivers swollen  
572 with snowmelt. The events of September 2013 add another chapter to this history for which  
573 the only comparable event was reported to have occurred in 1938. In a time of year when  
574 summer thunderstorms occur with less than half the frequency of June, July or August and cool-  
575 season “upslope” storms are not yet very common, many streams are typically beginning to run

576 dry before the onset of winter. Most of the region's inhabitants are used to enjoying  
577 shortening warm dry days and cool clear nights. September 2013, however, will hold different  
578 memories, when record heat abruptly turned to days of relentless rain that, in turn, brought  
579 water and hillsides down, rivers out of their banks, widespread destruction and tragic loss.

580

581 The synergy of the meteorological conditions witnessed during these events provides an  
582 opportunity to learn how extreme hydrometeorological events evolve as well as a critical  
583 chance to evaluate, improve and harden flood prediction and protection infrastructure. Of the  
584 over 400 mm of rainfall that fell in some locations, much of that rainfall was not well estimated  
585 using typical radar Z-R relationships or current polarimetric rainfall-rate retrieval algorithms.

586 Low cloud bases with a 2.5-km deep warm-cloud zone, terrain blockage in higher mountain  
587 areas, low evaporation rates, and a dominance of small raindrops at the surface, which was  
588 unusual for this particular region and season, resulted in nearly all operational QPE products  
589 significantly underestimating rainfall amounts. Numerical weather prediction models showed  
590 some skill in capturing the large-scale moisture advection features that would bring record  
591 atmospheric moisture levels and heavy rainfall to the region, but most of the operational  
592 models significantly underestimated total rainfall amounts and often possessed significant  
593 errors in predicting where heavy rainfall would occur. These findings on QPF performance are  
594 consistent with other recent reports including the NWS Service Assessment on the Sept. flood  
595 event. Owing partly to these deficiencies, advanced flood preparedness information was not  
596 available until the event actually began to unfold, particularly in headwater regions along the  
597 mountains. Until as little as 12 hours before the main flooding period, no flood or flash flood

598 watch was issued in the critically impacted areas of Boulder and Larimer counties on Sept. 11.  
599 though we note that a flash flood watch was issued for regions further south in Colorado .  
600 Lacking confident guidance in QPFs and QPEs, and associated streamflow forecasts, forecasters,  
601 emergency management personnel, researchers, the media and the public turned to local  
602 networks of surface observations for information as the event unfolded. Those networks  
603 provided invaluable information on where the heaviest rainfall and flooding was taking place  
604 until, in some cases, those instruments were destroyed during the event. It cannot be over-  
605 emphasized how much more dangerous this event would likely have been to the population  
606 without the information from these instrument networks feeding into local forecast offices,  
607 emergency response agencies, the media and the public alike, particularly in remote mountain  
608 locations.

609

610 This paper documents many aspects of the September flooding event and points the way to  
611 new observations and tools that potentially have significant value in the future. While  
612 operational radar products had difficulty in estimating rainfall during the event, research  
613 networks of surface disdrometers and vertically pointing radars were able to measure, in real-  
614 time, important raindrop-size distribution information and vertical profile of reflectivity  
615 information that may provide critical guidance for improving real-time rain rate estimates from  
616 radars. Systems, such as VDRAS, that can rapidly (e.g. approximately every 10 minutes)  
617 assimilate Doppler radar reflectivity and radial velocity data, offer an opportunity to provide  
618 frequent, high-resolution updates on evolving mesoscale winds, convergence and updraft  
619 regions. Such capabilities should lead to improved nowcasts and forecasts of precipitation.

620 Other advanced data assimilation systems, such as 3- and 4-dimensional variational systems or  
621 the Gridpoint Statistical Interpolation (GSI, 2014) system, with radar data assimilation also have  
622 the potential to yield improved forecasts of precipitation. New research weather forecast  
623 models such as the NOAA High Resolution Rapid Refresh (HRRR) model may offer new  
624 opportunities to rapidly assimilate such mesoscale information and improve short term QPFs.  
625 Similarly, new generations of spatially-continuous hydrological models that utilize new  
626 hydrologic data assimilation methodologies, as opposed to simpler point forecast models, should  
627 be able to provide additional information on the location and timing of floods in small  
628 headwater regions if more accurate rainfall estimates and forecasts can be provided. In  
629 addition to the challenges of rebuilding the communities destroyed by the floods, the challenge  
630 of improving regional observational and prediction systems is also set. As improved awareness  
631 of this poorly understood kind of flood risk settles in, so too must a renewed commitment to  
632 preparing ourselves for its eventual return.

633

634

635 [Sidebar 1: *Societal Impacts from September 2013 Colorado Floods*  
636 The September 2013 floods have left deep scars on the communities that lived through them.  
637 The final cost of the damage is still being tabulated but will likely exceed \$2 billion. The Table  
638 in this sidebar provides a basic summary of what these impacts were in terms of lives lost,  
639 communities disrupted and transportation corridors destroyed. Figure S1 illustrates a) the  
640 widespread nature of the 1,138 documented debris flows that occurred during this event (Coe  
641 et al., 2014) and b) the 18 counties that were declared by FEMA as federal disaster areas.]

642

643

644 [Sidebar 2: Record Rainfall

645 Several precipitation records were broken during the September 2013 event. A USGS rain  
646 gauge on Fort Carson, near Colorado Springs (south of the map shown in Figure 1), accumulated  
647 301 mm (11.85 inches) of rain from midnight to midnight local time of 12-13 September and  
648 316 mm (12.46 inches) from 9 AM 12 September to 9 AM on the 13<sup>th</sup> local time. This  
649 accumulation established a new daily rainfall extreme for the entire state of Colorado  
650 surpassing the long-standing gauge measurement of 281.4 mm (11.08 inches) on 17 Jun, 1965.  
651 The city of Boulder set several local station records for 1-day (230.6 mm or 9.08 inches), 2-day  
652 (292.6 mm or 11.52 inches), 3-day (341.8 or 13.44 inches), 7-day (429.3 mm or 16.9 inches) and  
653 monthly (461.2 mm of 18.16 inches) rainfall records. The city of Denver also set a precipitation  
654 accumulation record for the month of September (142.5 mm or 5.61 inches; NWS 2013b).  
655 Three of the top 10 largest 1-day rain events in state history will now be associated with the  
656 September 2013 storm. Additionally, according to analyses performed by the NOAA  
657 Hydrometeorological Design Center, the annual exceedence probability for the worst case 24-  
658 hour precipitation was estimated to be less than 1/1000 (NWS-2013a; Figure S2). This has led  
659 some to erroneously label the resulting flood as a “1000-year flood” event. However, return  
660 periods of rainfall events often do not directly relate to the return period of the resulting flood.  
661 Nevertheless, the heavy rainfall in the foothills and mountains resulted in over 1,100  
662 documented landslides (Sidebar 1: Coe et al. 2014) and led to incredible flood damage  
663 described below. END SIDEBAR 2]

664

665 [Sidebar 3: Raindrop structure and polarimetric radar data...  
666 The prevalence of small and nearly spherical raindrops are evident in the dual-polarization  
667 measurements from the CSU-CHILL radar as well as in disdrometer dropsize distributions  
668 derived using the transition (T-matrix) method (Waterman 1965; Mishchenko et al. 1996;  
669 Vivekanandan et al. 1991; Bringi and Chandrasekar 2001). Small, nearly spherical raindrops  
670 contribute comparatively little information to polarimetric radar signals such as differential  
671 reflectivity ( $Z_{dr}$ ) and specific differential phase shift ( $K_{dp}$ ).  $Z_{dr}$  values observed by the CSU-CHILL  
672 radar during the second episode (22-03 UTC on 12 Sep) were generally less than 1 dB though  
673 higher values were also observed (Figure Sidebar 3b). For the highest observed reflectivities of  
674 about 45 dBZ from the CSU-CHILL radar (Fig. Sidebar 3c), the mean observed  $Z_{dr}$  value is around  
675 1 dB. This approximately corresponds to the mean mass-weighted equivalent sphere drop  
676 diameter  $D_m \approx 0.16$  cm (1.6 mm) according to an average  $D_m$ - $Z_{dr}$  relation (e.g.,  $D_m$ (cm)  
677  $=0.16Z_{dr}^{0.49}$  (dB), Bringi and Chandrasekar 2001; Matrosov et al. 2006), and is in good  
678 agreement with the PARASIVE data (Fig. Sidebar 3b) and with the KFTG polarimetric data for  
679 periods when there is overlapping data. It is noted that larger  $Z_{dr}$  values (i.e., slightly larger,  
680 more oblate raindrops) were observed during the more convective times when rainfall rates  
681 exceeded 20 mm h<sup>-1</sup> (indicated by orange plus signs in Fig. Sidebar 3c). As a comparison, Fig.  
682 Sidebar 3b also shows the mean CSU-CHILL-derived  $Z$ - $Z_{dr}$  relation for a 12 July 2013 rainfall  
683 event with much higher mean  $Z_{dr}$  values ranging up to 2 dB, which is more typical for rainfall  
684 along the Colorado Front Range. This distinction between tropical-like, narrow drop size  
685 distributions and more typical diurnal convection drop size distributions, was noted by Bringi et  
686 al. 2001; Petersen et al. 1999 and Kennedy et al. 2001 in their respective analyses of other

687 events including the 1997 Ft. Collins flood event. Despite the small raindrops and low  
688 reflectivity, high values of  $K_{dp}/Z$  (where Z is in linear form) indicate large water contents with  
689 low reflectivity and small  $Z_{dr}$  values (Fig. Sidebar 3c). Due to the large concentration of small  
690 drops (and low  $Z_{dr}$  values) and the atypical Z-R relationship for the September Flood event, the  
691 operational single- and dual-polarization NEXRAD radar rainfall estimates had difficulty in  
692 developing accurate rainfall estimates. *END SIDEBAR 3]*

693

694

695 **Acknowledgements:**

696 We wish to extend our thanks to the following for their assistance in this article: The USGS,  
697 Colorado Division of Water Resources and Denver Urban Drainage and Flood Control District for  
698 streamflow and precipitation data; the U.S. National Weather Service, Northern Colorado  
699 Water Conservancy, Natural Resources Conservation Service Colorado Agricultural  
700 Meteorological network, and the CoCoRAHS network for precipitation data and other  
701 meteorological information; the Colorado Water Conservation Board for sharing peak flow  
702 information; Julie Meyer and Kevin Low of the NWS Missouri Basin River Forecast Center in  
703 Pleasant Hill, MO; Matt Bunkers for sharing the precipitable water information; Adam Smith of  
704 the National Climatic Data Center for the estimated damage costs resulting from the event.  
705 NARR analyses, radiosonde observations, and forecast model output were obtained from the  
706 National Climatic Data Center. Thanks to David Novak and Mark Klein for providing the  
707 archived WPC forecasts. We also extend our thanks to 3 anonymous reviewers and BAMS  
708 editor Jeff Waldstreicher for their constructive critiques of our original manuscript. The artful  
709 editorial contributions of Karen Griggs and Bobbetta Gochis are deeply appreciated. The views,  
710 opinions, and findings in this report are those of the authors, and should not be construed as an  
711 official NSF, NOAA or U.S. Government position, policy, or decision. Schumacher was partially  
712 supported by National Science Foundation grant AGS-1157425. This work was supported in  
713 part by the U.S. National Science Foundation through its support of NCAR.

714

715

716 REFERENCES

717 Boulder Area Sustainability Information Network (BASIN), 2014: Flood of 1938 – Eldorado  
718 Springs. Webpage available online at: <http://bcn.boulder.co.us/basin/history/1938flood.html>.

719

720 Bringi V.N. and V. Chandrasekar, 2001: Polarimetric Doppler Weather Radar. Cambridge  
721 University Press. 636 pp.

722

723 Bringi, V. N., V. Chandrasekar, J. Hubbert, E. Gorgucci, W. L. Randeu, M. Schoenhuber, 2003:  
724 Raindrop Size Distribution in Different Climatic Regimes from Disdrometer and Dual-Polarized  
725 Radar Analysis. *J. Atmos. Sci.*, 60, 354–365.

726

727 Caracena, F. , R. A. Maddox , L. R. Hoxit , and C. F. Chappell, 1979: Mesoanalysis of the Big  
728 Thompson Storm. *Mon. Wea. Rev.*, 107(1), 1-17.

729

730 Cifelli, R., V. Chandrasekar, S. Lim, P. C. Kennedy, Y. Wang, S. A. Rutledge, 2011: A New Dual-  
731 Polarization Radar Rainfall Algorithm: Application in Colorado Precipitation Events. *J. Atmos.*  
732 *Oceanic Technol.*, 28, 352–364.

733

734 Clark, R.A., J.J. Gourley, Z.L. Fleming, Y. Hong, E. Clark, 2014: CONUS-wide evaluation of  
735 National Weather Service flash flood guidance products. *Wea. and Forecasting*, in press.

736

737 Coe, J.A, J. W. Kean, J. W. Godt, R. L. Baum, E. S. Jones, D. J. Gochis, and G. S. Anderson, 2014:  
738 An extraordinary debris-flow event in the Colorado Front Range. *Geological Society of America*  
739 *Today*, In press. .

740

741 Crook, N. A, T. L. Clark, and M. W. Moncrieff, 1990: The Denver Cyclone. Part I: Generation in  
742 Low Froude Number Flow. *J. Atmos. Sci.*, 47, 2725–2742.

743

744 Gridpoint Statistical Interpolation (GSI) system, 2014: Documentation and code available online  
745 at: <http://www.dtcenter.org/com-GSI/users/>.

746

747 Hamill, T. M., 2014: Performance of operational model precipitation forecast guidance during  
748 the 2013 Colorado Front Range floods. *Mon. Wea. Rev.*, in press.

749

750 Hart, R. E., and R. H. Grumm, 2001: Using normalized climatological anomalies to rank synoptic-  
751 scale events objectively. *Mon. Wea. Rev.*, **129**, 2426–2442.

752

753 Houck, K. 2014: CDOT/CWCB Hydrology Investigation Phase One-2013 Flood Peak  
754 Determinations. State of Colorado official Memo.

755

756 Kitzmiller, D., D. Miller, R. Fulton, and F. Ding 2013: Radar and multisensor precipitation  
757 estimation techniques in National Weather Service hydrologic operations. *J. Hydrologic  
758 Engineering*, 18(2), 133-142.

759

760 Kennedy, Patrick C., Steven A. Rutledge, Walter A. Petersen, V. N. Bringi, 2001: Polarimetric  
761 Radar Observations of Hail Formation. *J. Appl. Meteor.*, 40, 1347–1366.

762

763 Lavers, D. A., and G. Villarini, 2013: Were global numerical weather prediction systems capable  
764 of forecasting the extreme Colorado rainfall of 9–16 September 2013?, *Geophys. Res. Lett.*, 40,  
765 doi:10.1002/2013GL058282.

766

767 Lin, Y., and K. E. Mitchell, 2005: The NCEP stage II/IV hourly precipitation analyses:  
768 Development and applications. Preprints, 19th Conf. on Hydrology, San Diego, CA, Amer.  
769 Meteor. Soc., 1.2. [Available online at <http://ams.confex.com/ams/pdffiles/83847.pdf>.]

770

771 Maddox, R.A., L. R. Hoxit, C. F. Chappell, and F. Caracena, 1978: Comparison of meteorological  
772 aspects of the Big Thompson and Rapid City flash floods. *Mon. Wea. Rev.*, 106, 375–389.

773

- 774 Maddox, R.A., 1980: Mesoscale Convective Complexes. *Bulletin of the American Meteorological*  
775 *Society*, 61(11), 1374-1387.
- 776
- 777 Matrosov, S.Y., R. Cifelli, P.C. Kennedy, S.W. Nesbitt, S.A. Rutledge, V.N. Bringi, and B.E.  
778 Martner, 2006: A comparative study of rainfall retrievals based on specific differential shifts at  
779 X- and S-band radar frequencies. *J. Atmos. Oceanic Technol.*, 23, 952-963.
- 780
- 781 Mesinger, F., and Coauthors, 2006: North American Regional Reanalysis. *Bull. Amer. Meteor.*  
782 *Soc.*, 87, 343–360.
- 783
- 784 Mishchenko, M.I., L.D. Travis, and D.W. Mackowski, 1996: T-matrix computations of light  
785 scattering by nonspherical particles: A review. *J. Quant. Spectrosc. Radiat. Transfer*, 55, 535-  
786 575.
- 787
- 788 Model Evaluation Tools (MET), 2014: The Meteorological Evaluation Tools verification software  
789 package. Code and documentation available online at: <http://www.dtcenter.org/met/users/>
- 790
- 791 Michaud, J.D., K.K. Hirschboeck and M. Winchell, 2001: Regional variations in small-basin floods  
792 in the United States. *Water Resources Res.*, 37(5), 1405-1416.

- 793
- 794 Moody, J.A., R.A. Shakesby, P.R. Robichaud, S.H. Cannon, D.A. Martin, 2013: Current research  
795 issues related to post-wildfire runoff and erosion processes. *Earth-Science Reviews*, 122, 10-37.
- 796
- 797 National Weather Service (NWS), 2014: The Record Front Range and Eastern Colorado Floods of  
798 September 11-17, 2013. U.S. Department of Commerce/National Oceanic and Atmospheric  
799 Administration Service Assessment. 74 pages. Available online at:  
800 [http://www.nws.noaa.gov/om/assessments/pdfs/14colorado\\_floods.pdf](http://www.nws.noaa.gov/om/assessments/pdfs/14colorado_floods.pdf)
- 801
- 802 National Weather Service (NWS), 2013a: Exceedence probability analysis for the Colorado Flood  
803 Event, 9-16 Sept. 2013. Hydrometeorological Design Studies Center (NWS-2013). Available  
804 online at: [http://www.nws.noaa.gov/oh/hdsc/aep\\_storm\\_analysis/8\\_Colorado\\_2013.pdf](http://www.nws.noaa.gov/oh/hdsc/aep_storm_analysis/8_Colorado_2013.pdf).
- 805
- 806 National Weather Service, 2013b: 2013 Annual climate summary for the Denver/Boulder  
807 Weather Forecast Office. Available online at:  
808 [http://www.crh.noaa.gov/bou/include/showProduct.php?product=denclm\\_2013.txt](http://www.crh.noaa.gov/bou/include/showProduct.php?product=denclm_2013.txt)
- 809
- 810 Petersen, W. A., L. D. Carey, S. A. Rutledge, J. C. Knievel, N. J. Doesken, R. H. Johnson, T. B.  
811 McKee, T. Vonder Haar, and J. F. Weaver, 1999: Mesoscale and radar observations of the Fort  
812 Collins Flash Flood of 28 July 1997. *Bull. Amer. Meteor. Soc.*, 80, 191-216.

- 813
- 814 Ryzhkov, A. V., S. E. Giangrande, and T. J. Schuur, 2005: Rainfall estimation with a polarimetric  
815 prototype of WSR-88D. *J. Appl. Meteor.*, 44, 502–515.
- 816
- 817 Schwarz, C., 2014: Reproducing the September 2013 record-breaking rainfall over the Colorado  
818 Front Range with High Resolution WRF model forecasts. *Weather and Forecasting, in press.*
- 819
- 820 Stewart, K., 2013: Information Services and Flood Warning Notes in *Flood Hazard News: An*  
821 *annual publication of the Denver Urban Drainage and Flood Control District*. 43, 14-25. Available  
822 online at: <http://www.udfcd.org/downloads/pdf/fhn/fhn2013/fhn2013.pdf>.
- 823
- 824 Sun J., and N. A. Crook, 1997: Dynamical and microphysical retrieval from Doppler radar  
825 observations using a cloud model and its adjoint: Part I. model development and simulated data  
826 experiments. *J. Atmos. Sci.*, 54, 1642-1661.
- 827
- 828 Szoke, E. J., M. L. Weisman, J. M. Brown, F. Caracena, and T. W. Schlatter, 1984: A subsynoptic  
829 analysis of the Denver tornado of 3 June 1981. *Mon. Wea. Rev.*, 112, 790-808.
- 830

831 Vivekanandan, J., W. M. Adams, and V. N. Bringi, 1991: Rigorous approach to polarimetric radar  
832 modeling of hydrometeor distributions. *J. Appl. Meteor.*, 30, 1053–1063.

833

834 Waterman, P.C., 1965: Matrix formulation of electromagnetic scattering. *Proc. IEEE*, 53, 805-  
835 812.

836

837 Wilczak, J. M., and T. W. Christian, 1990: Case Study of an Orographically Induced Mesoscale  
838 Vortex (Denver Cyclone). *Mon. Wea. Rev.*, 118, 1082–1102.

839

840 Yochum, S.E. and D.S. Moore, 2013: Colorado Front Range Flood of 2013: Peak flow estimates  
841 at selected mountain stream locations. Natural Resources Conservation Service, Technical  
842 Report, December, 2013.

843

844

845 **List of Figures**

846

847 **Figure 1.** Regional map of the Colorado Front Range. City names are in bold and indicated by  
848 red circles, river names are in black italics, county names are in grey italics. Red star is the  
849 location of the Denver NEXRAD radar (KFTG) and the orange star denotes the location of the  
850 CSU-CHILL radar. Numbers on the map correspond to peak flow measurement locations listed  
851 in Table 1. Some numbers lie on smaller streams not resolved in the map. USGS-defined wildfire  
852 perimeters shown in orange hatching.

853

854 **Figure 2.** September 9-17, 2013 total accumulated precipitation (mm) created with the Storm  
855 Precipitation Analysis System through a collaborative effort by Applied Weather Associates,  
856 LLC, MetStat, Inc. and Colorado Climate Center (Colorado State University). Dark red lines  
857 denote major roads and highways. Red dots approximate town and city center locations. White  
858 stars indicate locations of research laser disdrometers.

859

860 **Figure 3:** Timeline of September 2013 hydrometeorological event.

861

862 **Figure 4.** a) Time-mean 500-hPa geopotential height (black contours every 60 m) and anomaly  
863 (color shading in m); b) GOES-13 water vapor image , 500-hPa geopotential height (m), and 500-  
864 hPa wind vectors at 0600 UTC 12 September 2013; c) Column-integrated precipitable water  
865 (black contours every 5 mm) and standardized anomaly (color shading in units of standard  
866 deviations) for 12 September 2013; and d) 700-hPa zonal wind (black contours every 5  $m s^{-1}$  for  
867 values  $\leq 0$ ), wind barbs, and standardized anomalies (color shading). Atmospheric fields come  
868 from the North American Regional Reanalysis (NARR; Mesinger et al. 2006), and standardized  
869 anomalies were calculated using the method of Hart and Grumm (2001) with a 21-day window.

870

871 **Figure 5.** a) Precipitable water (PW, in cm) from the surface to 300 hPa as measured from  
872 radiosondes in Denver. Plotted are the daily means, maxima, minima, and one standard  
873 deviation above and below the means for days in September, based on climatological data from  
874 1946-2012 for September. Also plotted are the values measured in September 2013 (in  
875 black). Six consecutive soundings from 0000 UTC on 11 September to 1200 UTC on 13  
876 September set new single day PW records. The all-time Denver PW record from 11 July 1998 is  
877 also plotted for reference. b) Skew-T log p diagram of the sounding from Denver, Colorado at  
878 12 UTC on 1200 September 2013. The solid red line shows temperature and the solid green  
879 line dewpoint at this time. The solid black line shows the mean 1200 UTC temperature for  
880 September, the solid blue line shows the mean 1200 UTC September dewpoint, and the dashed  
881 blue line shows the mean dewpoint plus one standard deviation. These mean and standard

882 deviation calculations used observations from 1957-2012 and only mandatory levels. The  
883 1200 UTC 12 September 2013 sounding was launched into cloud and precipitation, which is  
884 representative of the widespread moist upslope conditions in Colorado during 11-13  
885 September, but may not be representative of the conditions in cloud-free areas.

886

887 **Figure 6.** Hovmoller (time-longitude) plots of Denver NEXRAD (KFTG) radar reflectivity for the  
888 area corresponding to Figure 2. a) 9-13 September, 2013, b) 11-13 September inset dashed line  
889 box in b) denotes period of heaviest rainfall and flash flooding. Solid arrows with letters  
890 indicate dominant directional movement of radar echoes ('W-E' is west to east, 'E-W' is east to  
891 west). The data are Level2 NEXRAD reflectivity data interpolated onto a 0.5 x 0.5 x 0.5 km<sup>3</sup>  
892 grid using the Radx software package. The mean topography averaged longitudinally (N-S) is  
893 shown along the bottom.

894

895 **Figure 7.** VDRAS wind analysis (2km MSL) at 22 UTC on 11 September and 00, 02, 04, 06 and 08  
896 UTC on 12 September. Static brown shading is topography and purple-to-yellow shading is  
897 observed reflectivity from a mosaic of the KFTG (Denver) and KCYS (Cheyenne) WSR-88D  
898 radars.

900

901 **Figure 8.** Time series of mean infrared brightness temperature from the GOES-13 satellite  
902 (black line) within a 10 km radius of Boulder, lightning source density within a 20 km radius  
903 around Boulder from the Colorado Lightning Mapping Array (green line), and rainfall rates (cm  
per hour) observed at Boulder and Sugarloaf (red lines).

904

905 **Figure 9.** Vertical cross section of a) reflectivity (Zh), b) Radial Doppler velocity (Vr), c)  
906 differential reflectivity (Zdr), d) specific differential phase (Kdp) and e) hydrometeor  
907 classification (HID) observed by the CSU-CHILL S-band radar on 12 September at 2323UTC. The  
908 radar was scanning towards the southwest (225°) from the radar location over a distance of  
909 approximately 90 km.

910

911 **Figure 10.** a) Vertical profile of Doppler velocity observed by a vertically-pointing micro rain  
912 radar (MRR). Approximate location of the melting layer is indicated by a dashed lines. MRR was  
913 located in Boulder, CO at 1.66 km MSL. b) Height of the lowest cloud base measured by a  
914 ceilometer. c) and d) Mean volume drop diameter and rainfall rate observed by surface  
915 disdrometers in Boulder and the Foothills. Note the Sugarloaf disdrometer was not operating  
916 between 08-18 UTC on 12 September and on 13 September. Black arrows in a and d indicate  
917 the time of the radar observations shown in Fig. 1. All data were plotted at 1-minute resolution.

918

919 **Figure 11.** Point-station comparisons of 2-day (00 UTC 11 through 00 UTC 13 September) total  
920 rainfall from five different QPE products and observations: (a) KFTG Default Z-R, (b) KFTG  
921 Tropical Z-R, (c) KFTG Dual-pol based estimates, (d) MPE, (e) Stage IV, and (f) observations.  
922 Observations consist of a combination of operational and research data networks and have  
923 been manually quality controlled. A summary of the 2-day total accumulation and bias for  
924 three enclosed regions (inset boxes) are given in Appendix D.

925

926 **Figure 12.** Point-station bias estimates of 2-day (00 UTC 11 through 00 UTC 13 September)  
927 estimated rainfall from a) KFTG Default Z-R, (b) KFTG Tropical Z-R, (c) KFTG Dual-pol based  
928 esimates, (d) MPE, and (e) Stage IV. The bias is computed from QPE minus observation.

929

930 **Figure 13.** Predicted and analyzed accumulated precipitation in the 48 hour period initialized  
931 from 0000 UTC 11 September from a) NCEP Global Forecast System (GFS), b) NCEP North  
932 American Model (NAM-12km), c) NCEP North American Model (NAM-4km), d) NCEP Short  
933 Range Ensemble Forecast (SREF) mean, e) ECMWF High Resolution (HRES) model, f) ECMWF  
934 Ensemble Prediction System (EPS) mean, g) NOAA Weather Prediction Center (WPC-human  
935 forecast) and h) NCEP Stage IV merged radar-gauge analysis. All forecasts and the analysis were  
936 regridded to a common 0.2° latitude/longitude grid.

937

938 **Figure 14.** NWS river stage forecasts (blue) and observations (black) for river locations with different  
939 relative response times: fast (top), medium (middle), slow (bottom).

940

941 **Figure A1:** Sea-surface temperature anomaly (deg C) for 9 Sep 2013. (Source: NOAA/NESDIS)

942

943 **Figure A2:** Normalized frequency of occurrence of hydrometeor classification by height (km) for the time  
944 period a) 02-05 Z using KFTG data and b) 21-24 UTC using CSU CHILL data. Big drops / melting hail and  
945 hail have frequencies smaller than 0.05% and are therefore shown in the subset axes to the right of each  
946 figure. [Although the same algorithm was used during both time periods, the polarized NEXRAD KFTG  
947 radar was used during the early period (02-05 UTC) due to lack of corresponding CSU CHILL data. The  
948 two radars have different scanning strategies, with the CSU CHILL radar performing fewer high elevation  
949 angles to capture the upper levels. The plots are gridded to the same horizontal domain centered on  
950 CHILL and facing west, with a 0.5 km horizontal and vertical resolution.]

951

952      **Figure A3.** Soil moisture values at 10cm and 60 cm depth from the U. of Colorado Mountain Research  
953      Station approximately 30 km west of Boulder, CO at 3,300 m MSL elevation. The period from 1 October  
954      2012 through 1 January 2014 is shown to illustrate that values observed during the September 2013  
955      floods were similar to saturated soil moisture conditions observed during peak snowmelt periods.

956

957      **Figure A4.** Flash Flood Guidance (FFG) from Upper Missouri River Basin Forecast Center (MBRFC) for  
958      four different forecast times from 9-13 September, 2013. Color shading indicates the threshold amount  
959      of rainfall (inches) required to generate significant flooding.

960

961

962

963      **Figure SB1.** Map of over 1,100 documented hillslope failures by Jonathan Godt and Geff Coe of USGS.  
964      Green dots are location and proportional size of hillslope failures, yellow shading denotes city areas, red  
965      shading outlines region of heave rainfall, brown shading outlines regions of recent wildland fires, b)  
966      FEMA Map of Colorado Disaster county declarations.

967

968      **Figure SB2.** 9-16 September Annual Exceedance Probabilities for worst case 24-hour rainfall. (NWS  
969      2013).

970

971      **Figure SB3.** Scatterplots showing ratios of a) disdrometer-based Z-R, and b) Zdr-Z relationship based on  
972      CHILL radar observations, c) disdrometer-based Kdp/Z-Zdr relationship. Disdrometer data is based on  
973      period shown in Fig. 6 (30 hours). CSU-CHILL radar data were analyzed between 1550 UTC 12 Sep until  
974      0240 UTC 13 Sep. a) and c) data are based on measurements at Boulder, Melvina Hill, and Sugarloaf.  
975      Red, green, and purple lines in a) represent Z-R relationships for the flood event based on three  
976      disdrometers, tropical rainfall, and non-tropical convective precipitation used by the WSD-88D radar,  
977      respectively. b) Green and black line represent typical mean values for a typical warm season rain event  
978      in the Front Range and for the Sept. 2013 flood event. Orange 'X's' in c) represent times when rainfall  
979      exceeded 20 mm h<sup>-1</sup>.

980

981

982 **List of Tables:**

983 **Table 1: Peak streamflow (cubic feet per second-cfs and cubic meters per second-cms), unit discharge**  
 984 **and event probability estimates compiled from available reports as of the writing of this paper. NRCS-**  
 985 **Yochum and Moore (2013); CWC-B-Houck, 2014; CWC-B-Colorado Water Conservation Board**  
 986 **preliminary peak flow report memo.**

Streamflow Station	Estimated		Basin Area sq mi (sq km)	Estimated		
	Estimated Peak Flow cfs (cms)	Unit Discharge cfs / sq mi (cms/ sq km)		Event Probability (%)		
					Source	
1. Coal Creek at Plainview	3900 (110)	258 (2.82)	15.1 (39.1)	> 1%	CWCB	
<b>Boulder Creek</b>						
2. Fourmile Creek at Orodell	2733 (77.4)	112 (1.24)	24.2 (62.7)	n/a	CWCB	
3. Boulder Creek at Orodell	2020 (57.2)	19.8 (0.22)	102 (264)	n/a	CWCB	
4. Boulder Creek at 28th Street	5300 (150)	39.0 (0.43)	136 (352)	4%	CWCB	
<b>James &amp; Lefthand Creeks</b>						
5. James Creek at Jamestown	4800 (136)	350 (3.8)	13.7 (35.5)	0.30%	NRCS	
6. Little James upstream of Jamestown	1800 (51.0)	578 (6.3)	3.11 (8.05)	0.30%	NRCS	
7. Lefthand at mouth	3520 (99.7)		n/a	1%	CWCB	
<b>St. Vrain River</b>						
8. Middle St. Vrain above S. St. Vrain	1750 (49.6)	54 (0.59)	32.4 (83.9)	1-2%	CWCB	
9. South St. Vrain at Middle St. Vrain	2700 (76.5)	40 (0.44)	66.7 (173)	2%	CWCB	
10. South St. Vrain above North St. Vrain	9000 (255)	98 (1.1)	92 (238)	>0.2%	CWCB	
11. North St. Vrain above South St. Vrain	12300 (348)	98 (1.1)	125 (323)	<0.2%	CWCB	
12. St. Vrain at Lyons	19600 (555)	90 (0.99)	216 (559)	>0.2%	CWCB	
13. St. Vrain at Interstate 25	18000 (509)	21 (0.23)	854 (2211)	<1%	CWCB	
<b>Little Thompson</b>						
14. Little Thompson at Pinewood Spgs	14600 (413)	314 (3.4)	46.4 (120)	0.33%	NRCS	
15. Little Thompson at Interstate 25	14500 (411)	85 (0.9)	170 (440)	0.20%	CWCB	
<b>Big Thompson</b>						
16. Fish Creek near Estes Park	6900 (195)	442 (4.8)	15.6 (40.4)	0.20%	NRCS	
17. Fall River upstream of Estes Park	3800 (108)	104 (1.1)	36.5 (94.5)	0.50%	NRCS	
18. Big Thompson at Drake above N. Fork	12500 (354)	65 (0.7)	191 (495)	0.20%	CWCB	
19. Big Thompson below Drake	29500 (835)	107 (0.7)	274 (709)	0.20%	CWCB	
20. North Fork Big Thompson at Drake	18400 (521)	259 (1.2)	70.9 (184)	0.40%	CWCB	
21. North Fork Big Thompson near Glen Haven	1700 (48.1)	93 (2.8)	18.2 (47.1)	1-2%	NRCS	
22. Buckhorn Creek at Masonville	11000 (311)	124 (1.3)	88.2 (228)	1-2%	NRCS	
<b>Cache la Poudre</b>						
23. Skin Gulch upstream fo Stove Prairie Road	2500 (70.8)	714 (7.8)	3.5 (9.06)	0.20%	NRCS	
24. Young Gulch upstream of CO-14	1200 (34.0)	79.0 (1.4)	15.2 (39.4)	2-4%	NRCS	
<b>South Platte River</b>						
25. South Platte at Ft. Lupton	10100 (286)	2 (0.02)	5043 (13056)	10%	CWCB	
26. South Platte at Kersey	55000 (1557)	5.7 (0.06)	9659 (25007)	0.20%	CWCB	

988   **Table A1:** Two-day total (00 UTC 11 — 00 UTC 13 September) rainfall from gauge observations (Obs.)  
 989   and five QPE products as well as the QPE bias for regions 1 — 3 shown on Figs. 12 — 13. The QPE bias is  
 990   computed from QPE minus observation. Values in parentheses indicate the number of gauges used for  
 991   the QPE evaluation.

992

**Region 1 (78)**

	Obs.	Stage IV	MPE	NEXRAD Default Z-R	NEXRAD Tropical Z-R	Dual-pol. NEXRAD
2-day total (mm)	76.0	87.6	76.2	30.5	121.1	50.9
Bias (mm)		8.0	-1.5	-46.1	38.3	-26.1

**Region 2 (69)**

	Obs.	Stage IV	MPE	NEXRAD Default Z-R	NEXRAD Tropical Z-R	Dual-pol. NEXRAD
2-day total (mm)	200.0	120.7	162.9	46.7	201.4	103.9
Bias (mm)		-74.3	-22.0	-140.8	8.5	-81.3

**Region 3 (87)**

	Obs.	Stage IV	MPE	NEXRAD Default Z-R	NEXRAD Tropical Z-R	Dual-pol. NEXRAD
2-day total (mm)	74.0	65.2	71.2	17.1	94.3	42.5
Bias (mm)		-13.2	-1.2	-57.8	14.4	-36.1

993

994

995

996

997

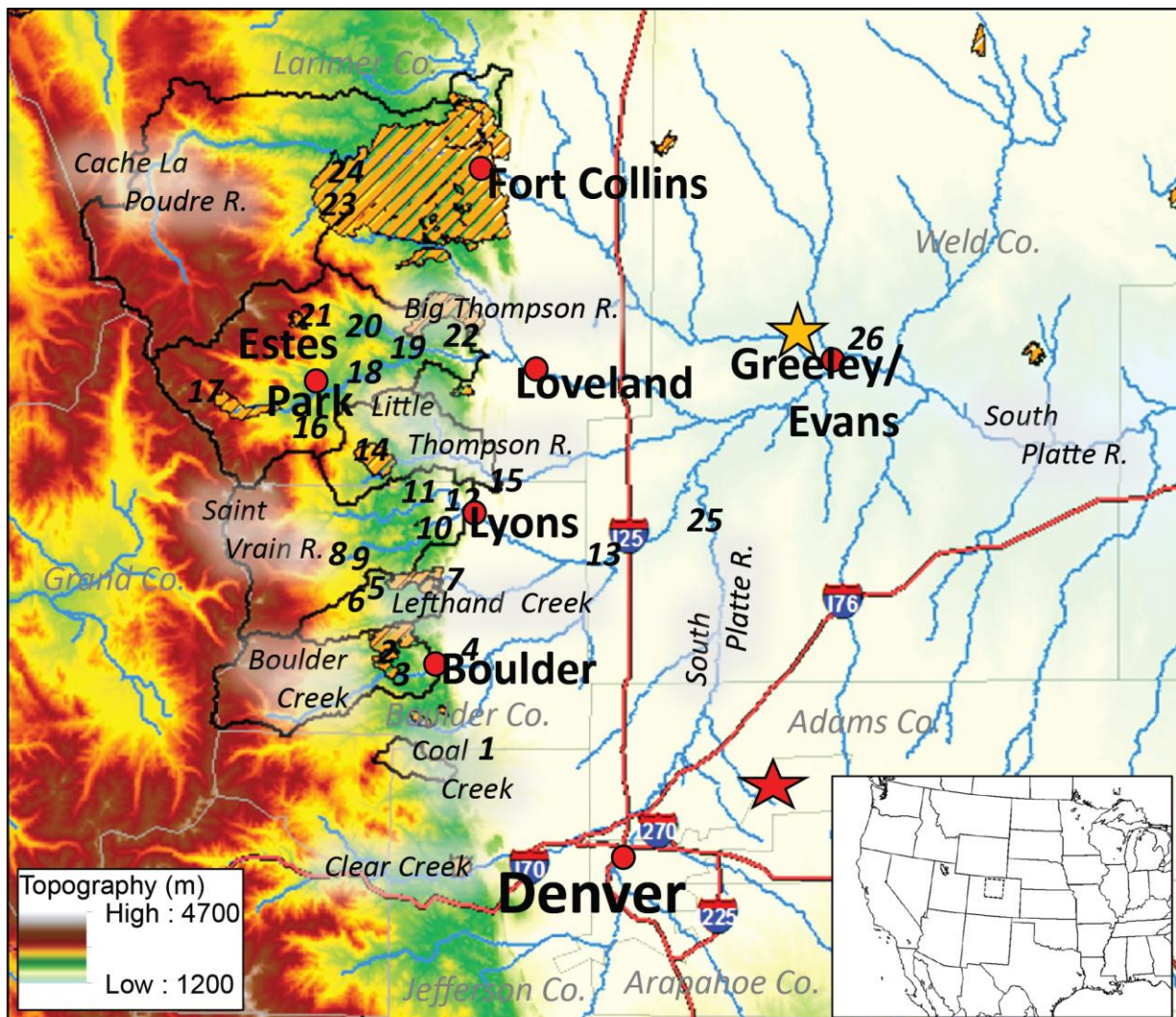
998 **Table SB1. List of impacts from the Great Colorado Floods of 2013**

<b>Selected Impacts from the September 2013 Colorado Floods</b>	
1.	There were 8 flood-related fatalities (NWS, 2014)
2.	Emergency evacuation and civil protection operations were activated on Sept. 12, 2013
3.	Colorado and Wyoming National Guards in coordination with the Department of Defense personnel from Fort Carson (4th Infantry) and Buckley Air Force Base evacuated more than 3,700 people from flooded communities
4.	Over 18,000 people were forced to leave their homes due to the flooding (FEMA)
5.	Over 1100 landslide and hillslope failures occurred during the event which have been implicated in 3 of the 10 fatalities (Coe et al. 2014 – Sidebar Figure S1a)
6.	Flooding destroyed at least 1,882 structures (FEMA)
7.	\$9M of FEMA money was used for basic first responder activities (FEMA)
8.	An official Federal Disaster was declared Sept. 14, 2013 (FEMA)
9.	18 counties were designated for Public Assistance- Adams, Arapahoe, Boulder, Clear Creek, Crowley, Denver, El Paso, Fremont, Gilpin, Jefferson, Lake, Larimer, Lincoln, Logan, Morgan, Sedgwick, Washington and Weld (Fig S1b) (FEMA)
10.	More than 28, 000 people registered for state and federal assistance, and more than 21,000 people visited disaster recovery centers
11.	National Flood Insurance Program approved more than \$55.7M claims
12.	As of Dec. 20, 2013, the Federal Emergency Management Administration (FEMA) has distributed \$204M to individuals and households, \$28M to repair infrastructure
13.	Over \$90M in Small Business Administration loans to businesses and non-profits and local governments
14.	Statewide, 485 miles of damaged or destroyed highways (CDOT news release webpage: <a href="http://www.coloradodot.info/news/2013-news-releases/11-2013/gov-hickenlooper-announces-all-damaged-highways-will-reopen-before-thanksgiving">http://www.coloradodot.info/news/2013-news-releases/11-2013/gov-hickenlooper-announces-all-damaged-highways-will-reopen-before-thanksgiving</a> )
15.	Of the 18 counties designated for assistance, Boulder County was hardest hit in terms of damages receiving more than \$33M in State and Federal reconstruction grants (FEMA), and over 150 miles of road were destroyed in Boulder Co alone (Sept. 28 Daily Camera)

999

1000

1001



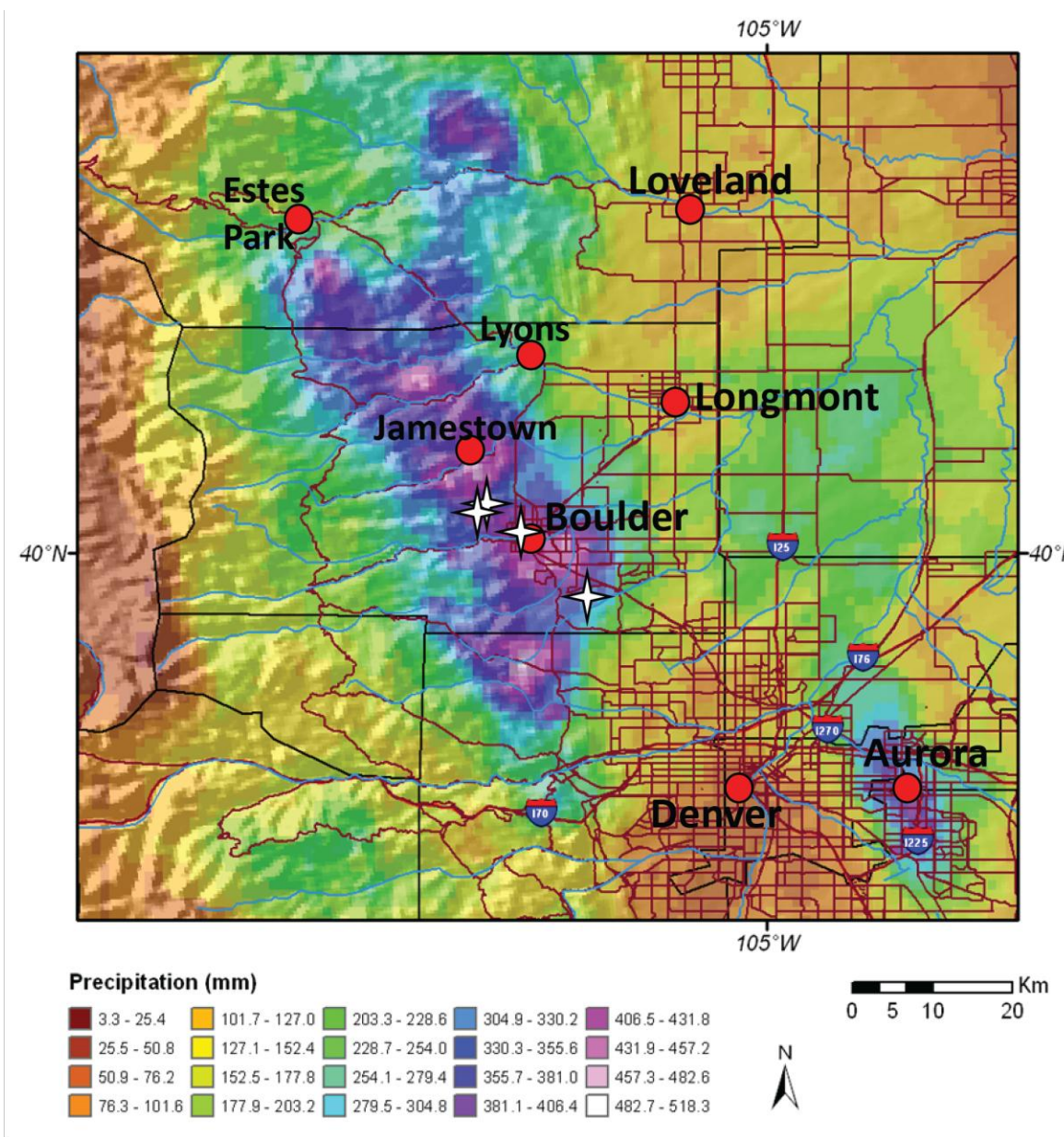
1002

1003

1004 **Figure 1.** Regional map of the Colorado Front Range. City names are in bold and indicated by  
 1005 red circles, river names are in black italics, county names are in grey italics. Red star is the  
 1006 location of the Denver NEXRAD radar (KFTG) and the orange star denotes the location of the  
 1007 CSU-CHILL radar. Numbers on the map correspond to peak flow measurement locations listed  
 1008 in Table 1. Some numbers lie on smaller streams not resolved in the map. USGS-defined wildfire  
 1009 perimeters shown in orange hatching.

1010

1011

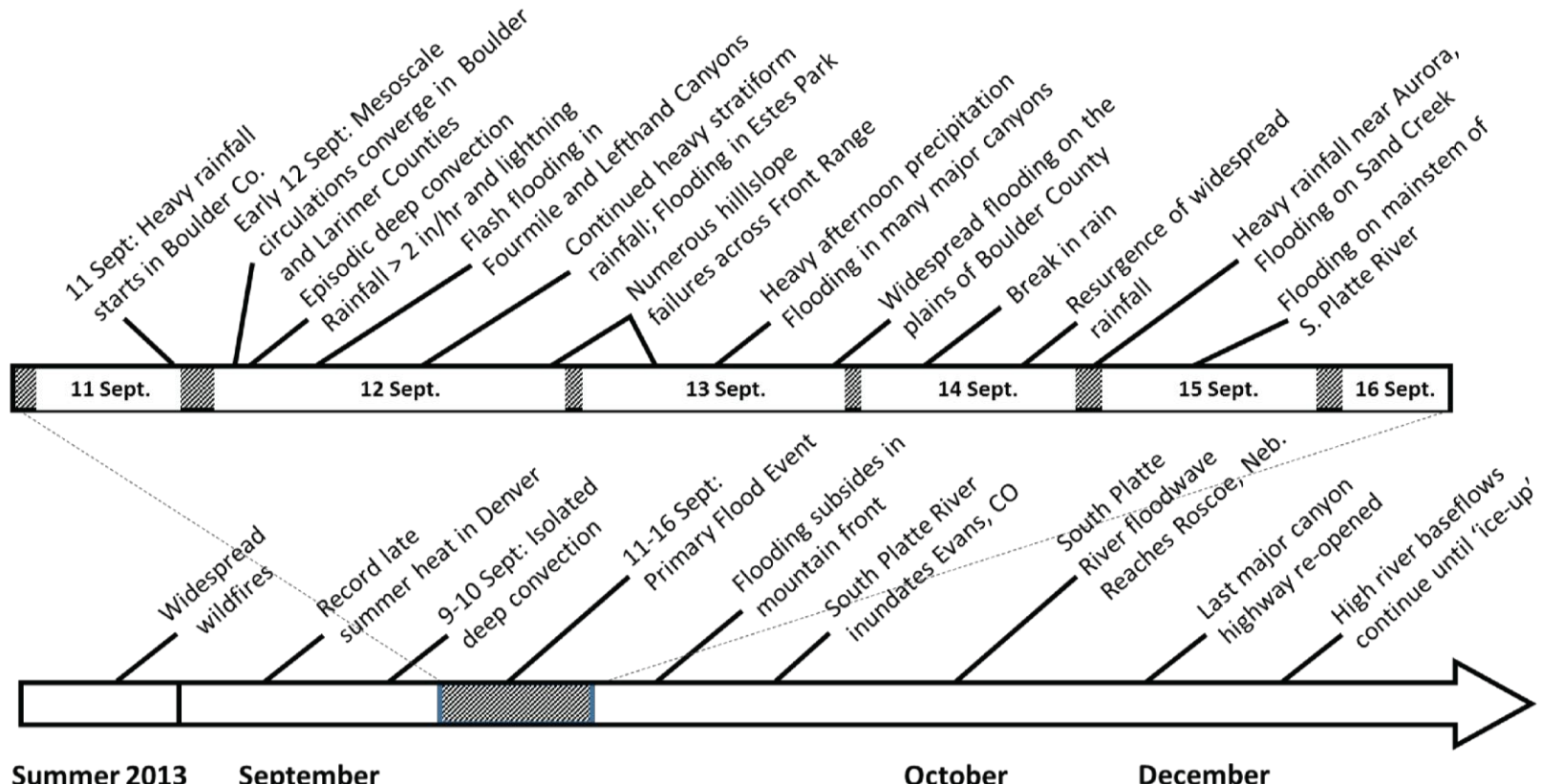


1012

1013

1014 **Figure 2.** . September 9-17, 2013 total accumulated precipitation (mm) created with the Storm  
 1015 Precipitation Analysis System through a collaborative effort by Applied Weather Associates,  
 1016 LLC, MetStat, Inc. and Colorado Climate Center (Colorado State University). Dark red lines  
 1017 denote major roads and highways. Red dots approximate town and city center locations. White  
 1018 stars indicate locations of research laser disdrometers.

1019

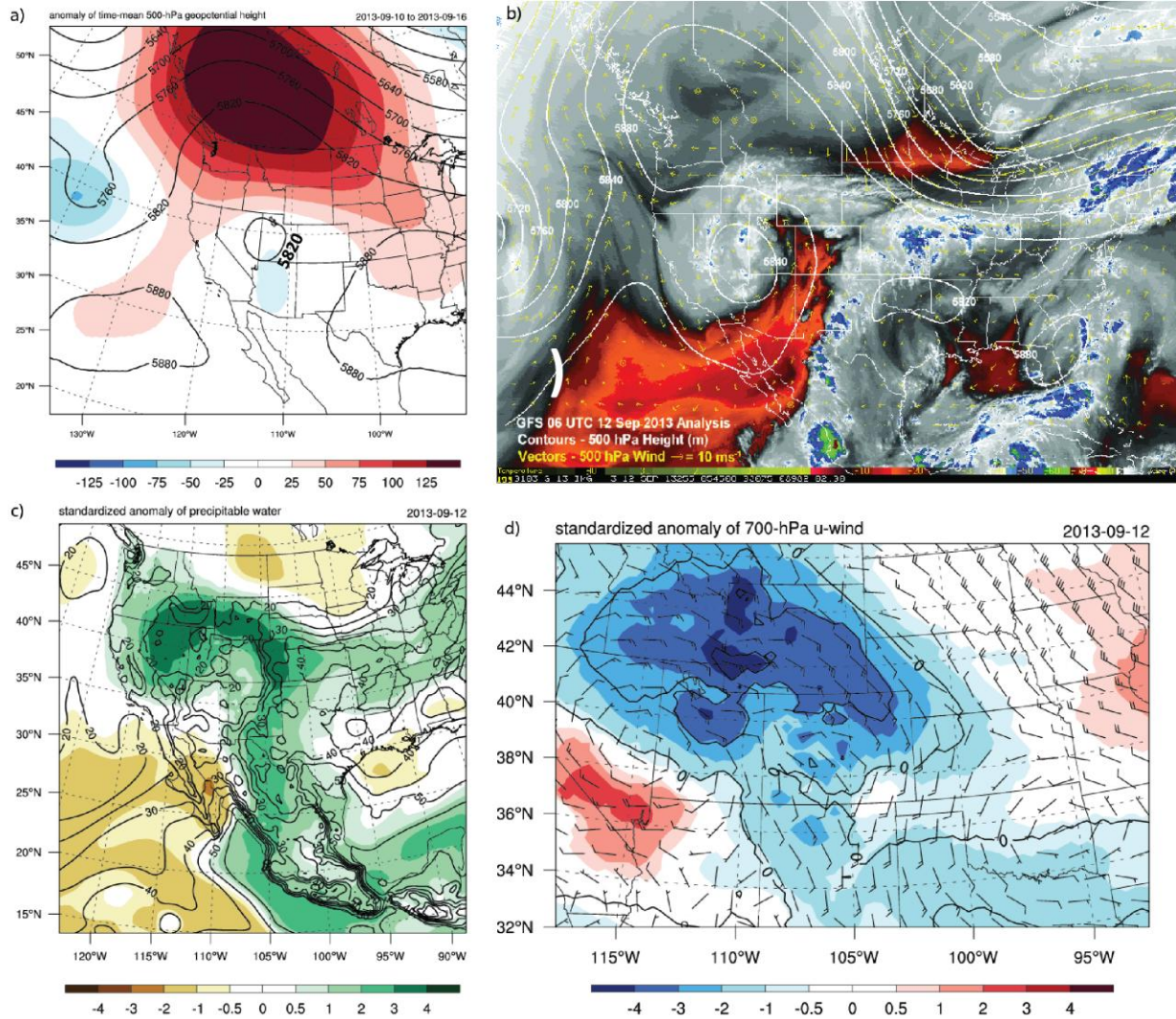


1020

1021

1022 **Figure 3:** Timeline of September 2013 hydrometeorological event.

1023

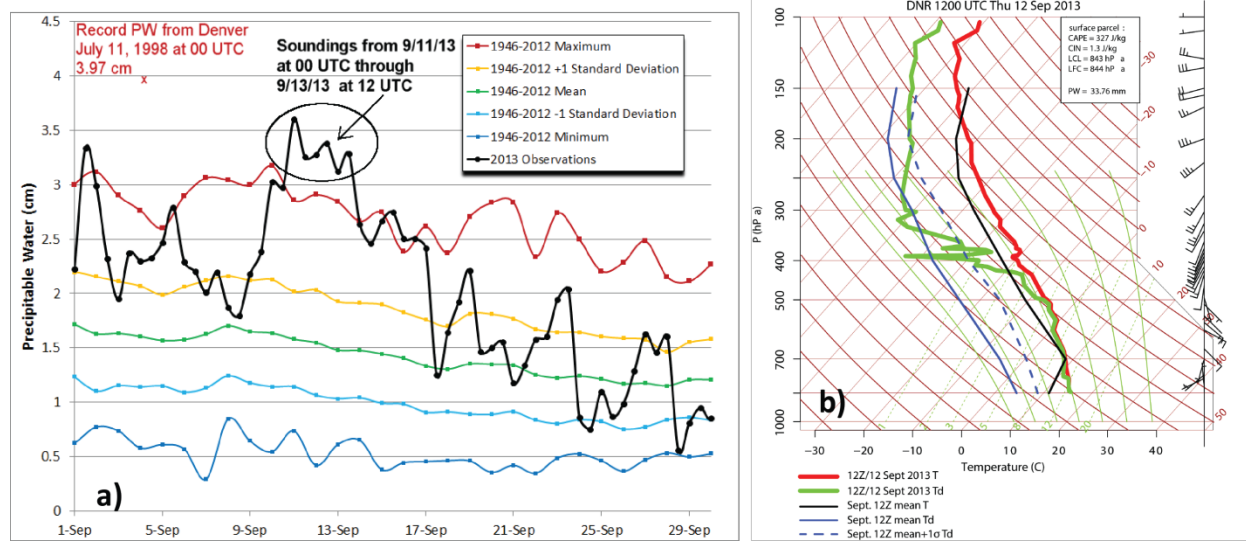


1024

1025

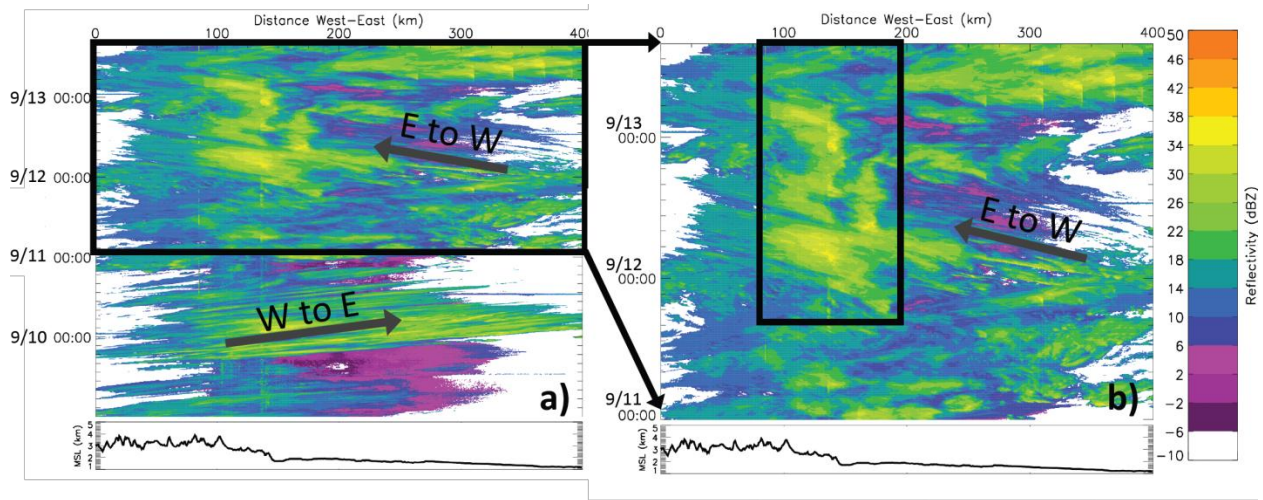
1026 **Figure 4.** a) Time-mean 500-hPa geopotential height (black contours every 60 m) and anomaly  
 1027 (color shading in m); b) GOES-13 water vapor image , 500-hPa geopotential height (m), and 500-  
 1028 hPa wind vectors at 0600 UTC 12 September 2013; c) Column-integrated precipitable water  
 1029 (black contours every 5 mm) and standardized anomaly (color shading in units of standard  
 1030 deviations) for 12 September 2013; and d) 700-hPa zonal wind (black contours every  $5 \text{ m s}^{-1}$  for  
 1031 values  $\leq 0$ ), wind barbs, and standardized anomalies (color shading). Atmospheric fields come  
 1032 from the North American Regional Reanalysis (NARR; Mesinger et al. 2006), and standardized  
 1033 anomalies were calculated using the method of Hart and Grumm (2001) with a 21-day window.

1034



1038 **Figure 5.** a) Precipitable water (PW, in cm) from the surface to 300 hPa as measured from  
1039 radiosondes in Denver. Plotted are the daily means, maxima, minima, and one standard  
1040 deviation above and below the means for days in September, based on climatological data from  
1041 1946-2012 for September. Also plotted are the values measured in September 2013 (in  
1042 black). Six consecutive soundings from 0000 UTC on 11 September to 1200 UTC on 13  
1043 September set new single day PW records. The all-time Denver PW record from 11 July 1998 is  
1044 also plotted for reference. b) Skew-T log p diagram of the sounding from Denver, Colorado at  
1045 12 UTC on 1200 September 2013. The solid red line shows temperature and the solid green  
1046 line dewpoint at this time. The solid black line shows the mean 1200 UTC temperature for  
1047 September, the solid blue line shows the mean 1200 UTC September dewpoint, and the dashed  
1048 blue line shows the mean dewpoint plus one standard deviation. These mean and standard  
1049 deviation calculations used observations from 1957-2012 and only mandatory levels. The  
1050 1200 UTC 12 September 2013 sounding was launched into cloud and precipitation, which is  
1051 representative of the widespread moist upslope conditions in Colorado during 11-13  
1052 September, but may not be representative of the conditions in cloud-free areas.

1054



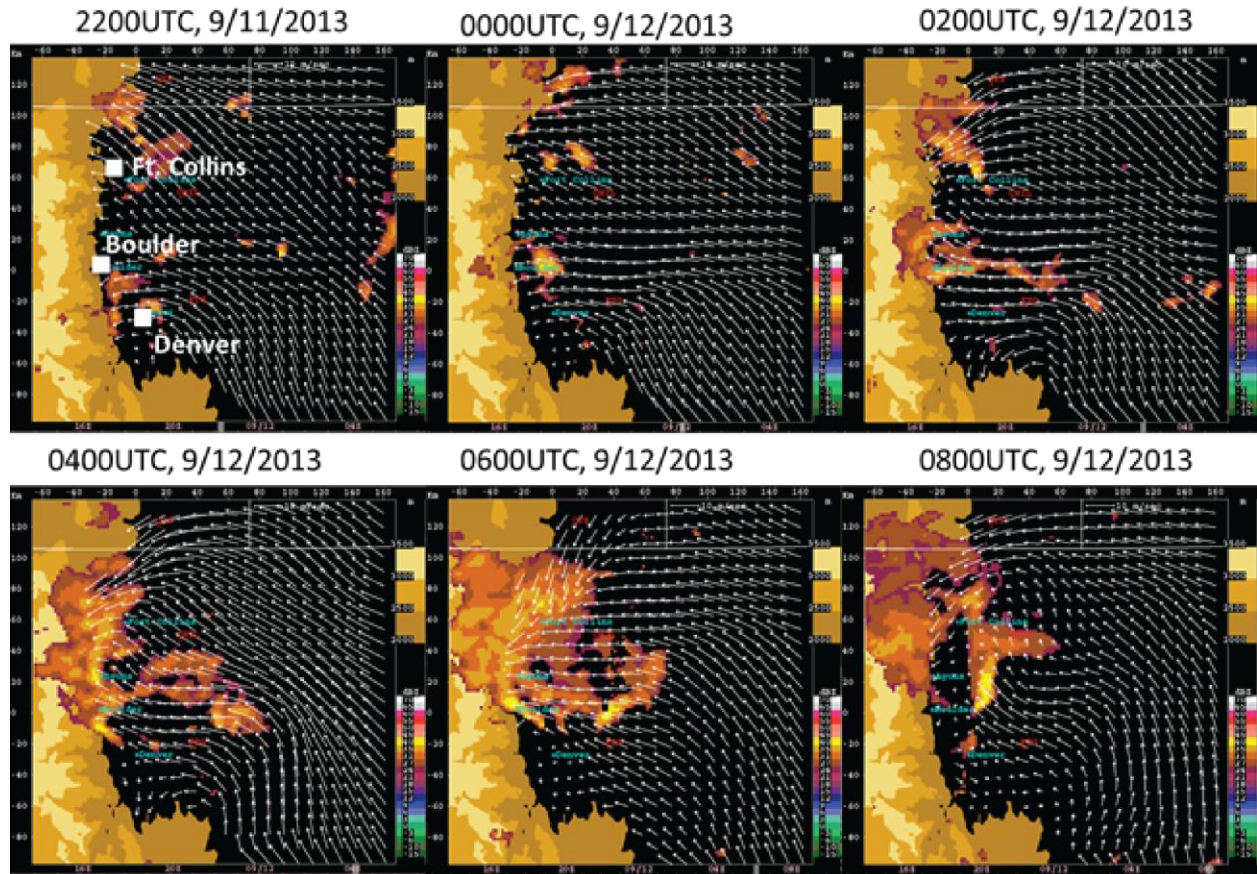
1055

1056

1057 **Figure 6.** Hovmoller (time-longitude) plots of Denver NEXRAD (KFTG) radar reflectivity for the  
1058 area corresponding to Figure 2. a) 9-13 September, 2013, b) 11-13 September inset dashed line  
1059 box in b) denotes period of heaviest rainfall and flash flooding. Solid arrows with letters  
1060 indicate dominant directional movement of radar echoes ('W-E' is west to east, 'E-W' is east to  
1061 west). The data are Level2 NEXRAD reflectivity data interpolated onto a  $0.5 \times 0.5 \times 0.5 \text{ km}^3$   
1062 grid using the Radx software package. The mean topography averaged longitudinally (N-S) is  
1063 shown along the bottom.

1064

1065



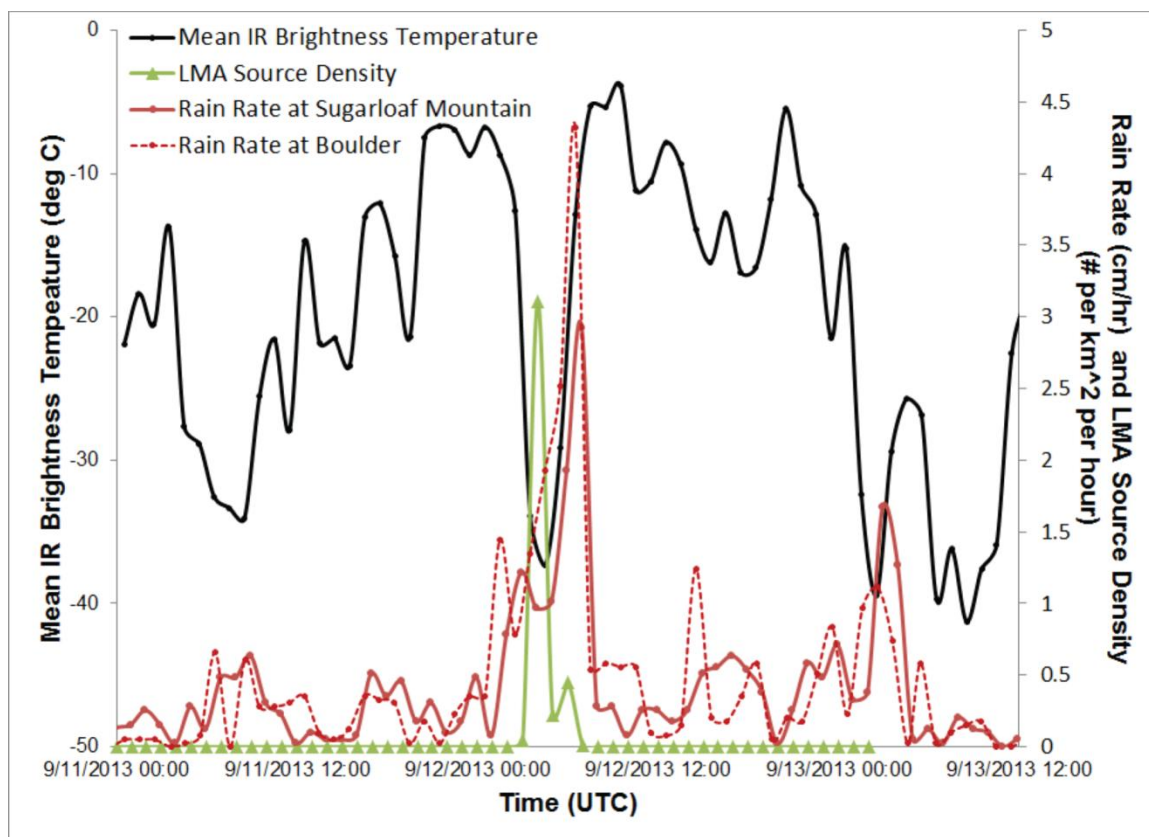
1066

1067

1068 **Figure 7.** VDRAS wind analysis (2km MSL) at 22 UTC on 11 September and 00, 02, 04, 06 and 08  
1069 UTC on 12 September. Static brown shading is topography and purple-to-yellow shading is  
1070 observed reflectivity from a mosaic of the KFTG (Denver) and KCYS (Cheyenne) WSR-88D  
1071 radars.

1072

1073



1074

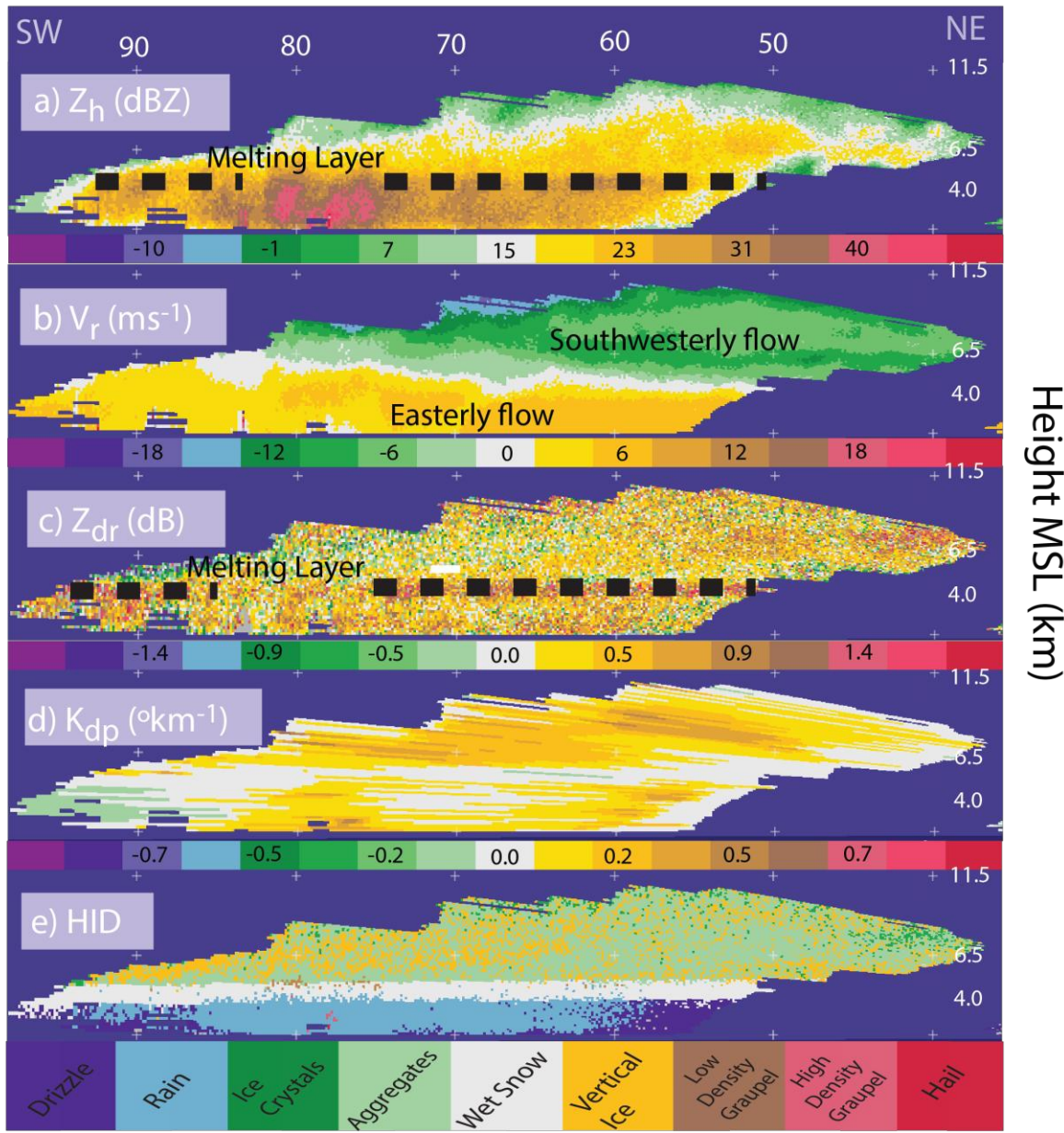
1075

1076 **Figure 8.** Time series of mean infrared brightness temperature from the GOES-13 satellite  
1077 (black line) within a 10 km radius of Boulder, lightning source density within a 20 km radius  
1078 around Boulder from the Colorado Lightning Mapping Array (green line), and rainfall rates (cm  
1079 per hour) observed at Boulder and Sugarloaf (red lines).

1080

1081

### Distance from the CSU-CHILL radar (km)

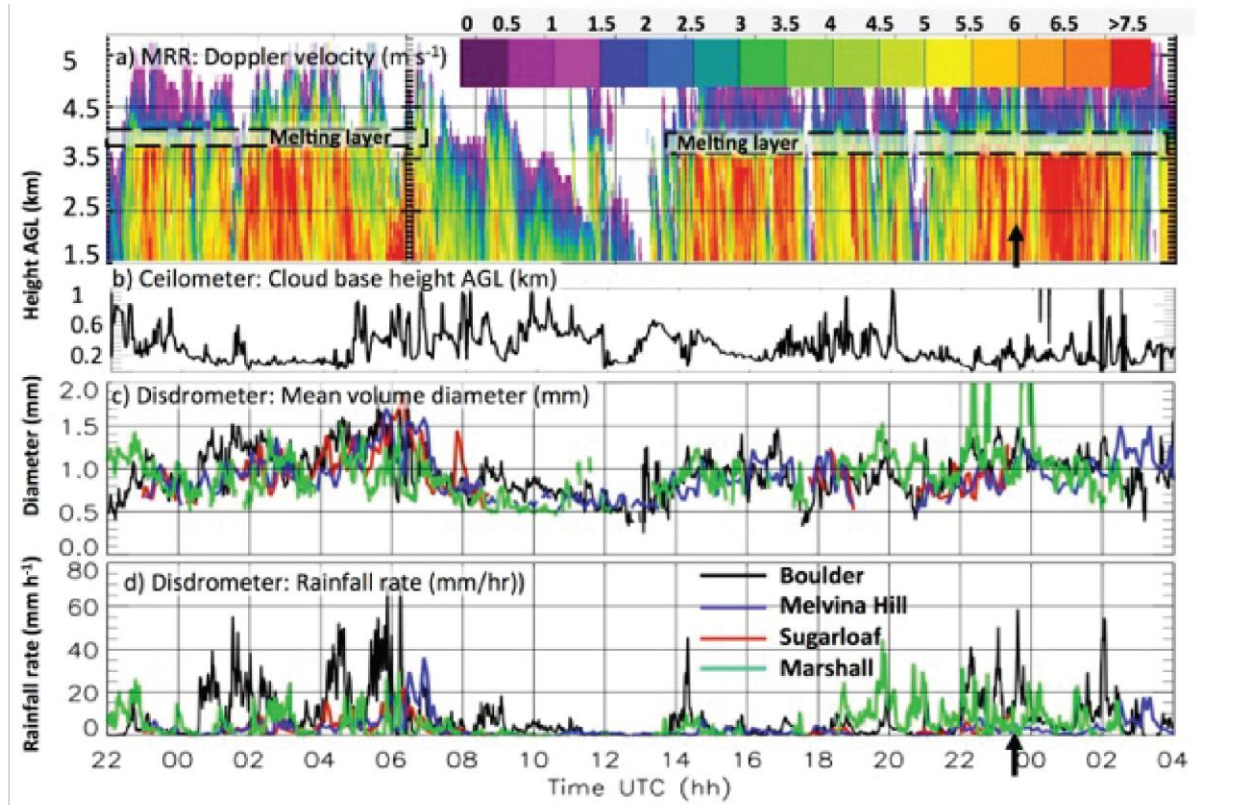


1082

1083

1084 **Figure 9.** Vertical cross section of a) reflectivity ( $Z_h$ ), b) Radial Doppler velocity ( $V_r$ ), c)  
 1085 differential reflectivity ( $Z_{dr}$ ), d) specific differential phase ( $K_{dp}$ ) and e) hydrometeor  
 1086 classification (HID) observed by the CSU-CHILL S-band radar on 12 September at 2323UTC. The  
 1087 radar was scanning towards the southwest ( $225^{\circ}$ ) from the radar location over a distance of  
 1088 approximately 90 km.

1089



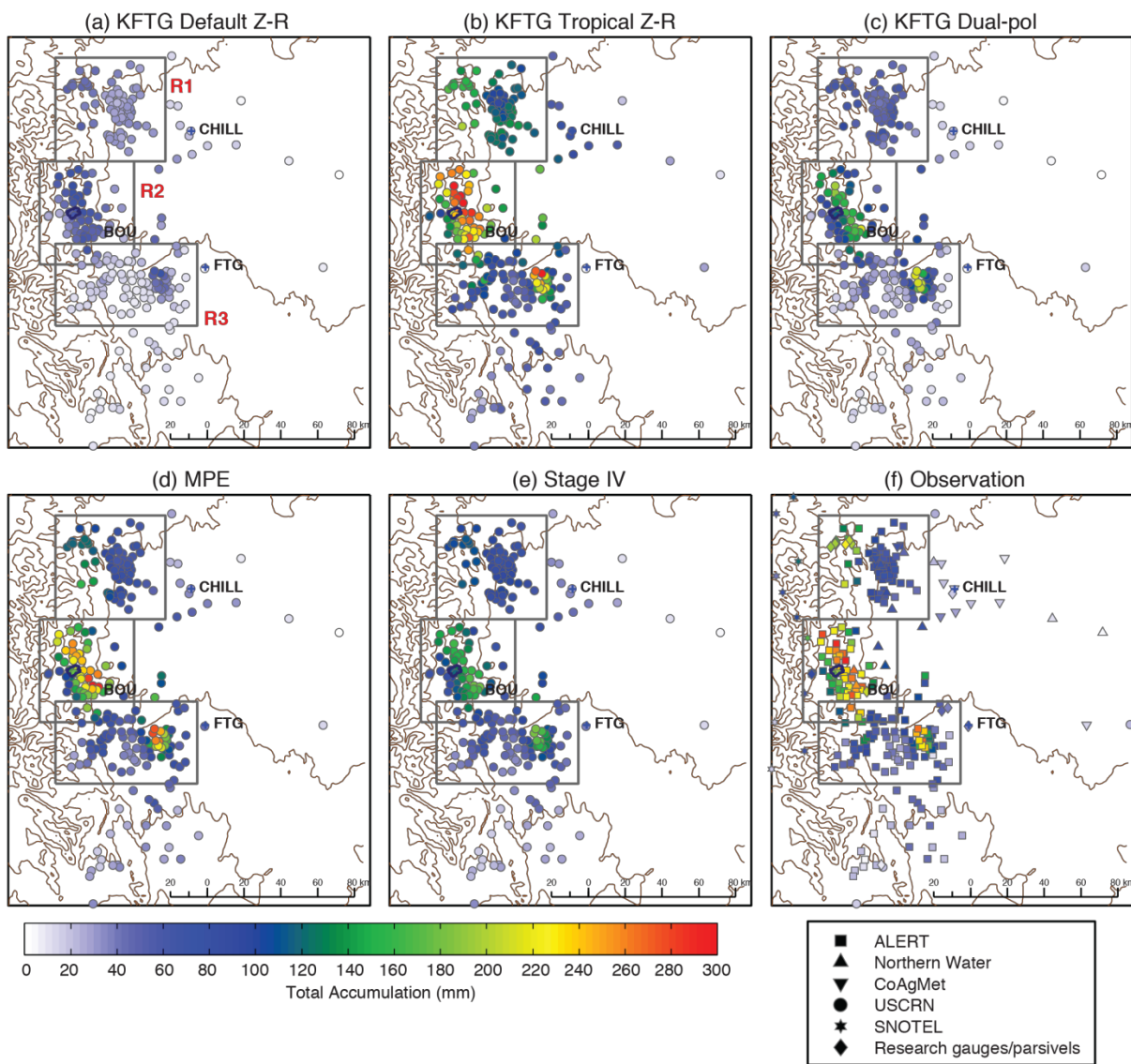
1090

1091

1092 **Figure 10.** a) Vertical profile of Doppler velocity observed by a vertically-pointing micro rain  
1093 radar (MRR). Approximate location of the melting layer is indicated by a dashed lines. MRR was  
1094 located in Boulder, CO at 1.66 km MSL. b) Height of the lowest cloud base measured by a  
1095 ceilometer. c) and d) Mean volume drop diameter and rainfall rate observed by surface  
1096 disdrometers in Boulder and the Foothills. Note the Sugarloaf disdrometer was not operating  
1097 between 08-18 UTC on 12 September and on 13 September. Black arrows in a and d indicate  
1098 the time of the radar observations shown in Fig. 1. All data were plotted at 1-minute resolution.

1099

1100



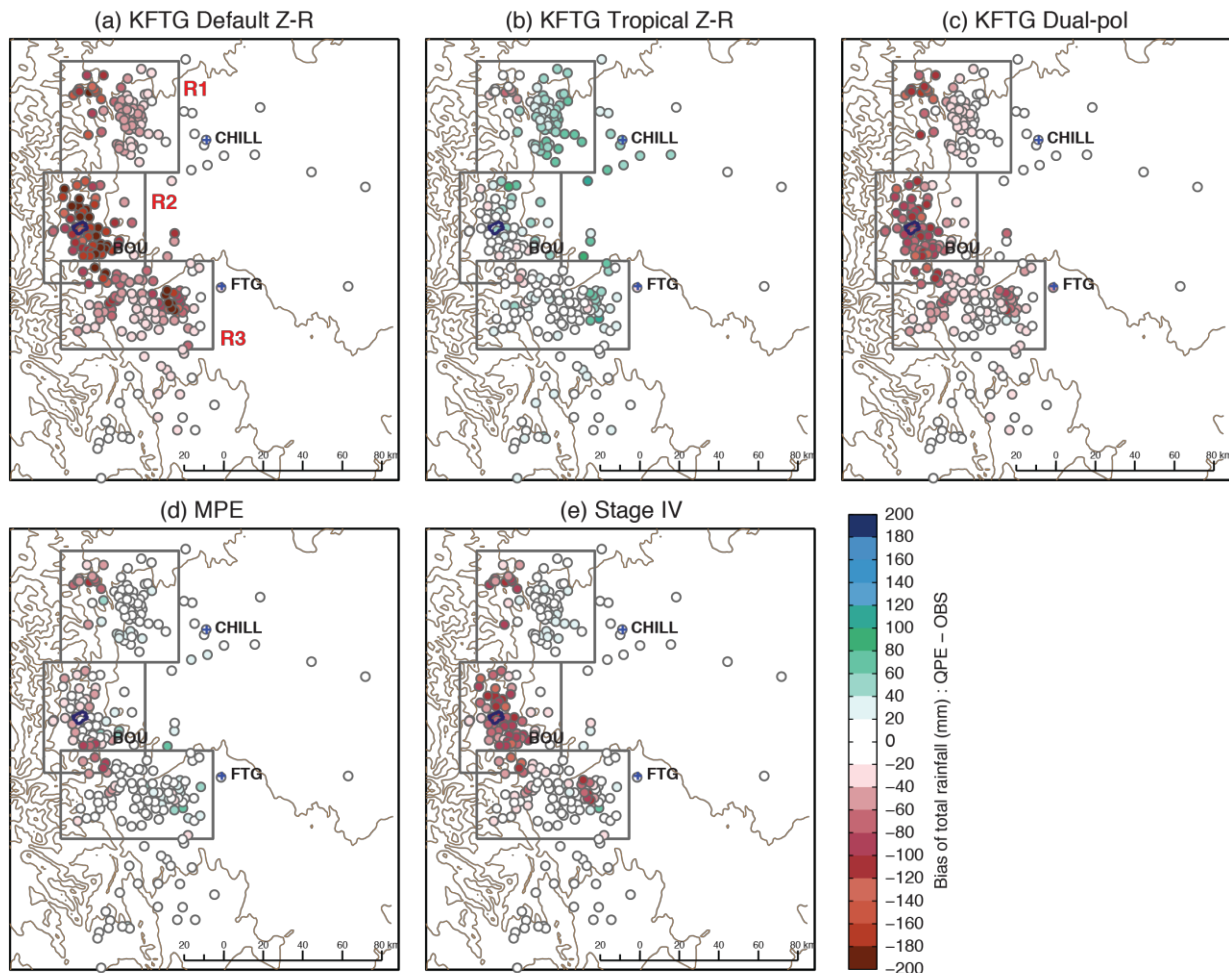
1101

1102

1103 **Figure 11.** Point-station comparisons of 2-day (00 UTC 11 through 00 UTC 13 September) total  
 1104 rainfall from five different QPE products and observations: (a) KFTG Default Z-R, (b) KFTG  
 1105 Tropical Z-R, (c) KFTG Dual-pol based estimates, (d) MPE, (e) Stage IV, and (f) observations.  
 1106 Observations consist of a combination of operational and research data networks and have  
 1107 been manually quality controlled. A summary of the 2-day total accumulation and bias for  
 1108 three enclosed regions (inset boxes) are given in Appendix D.

1109

1110



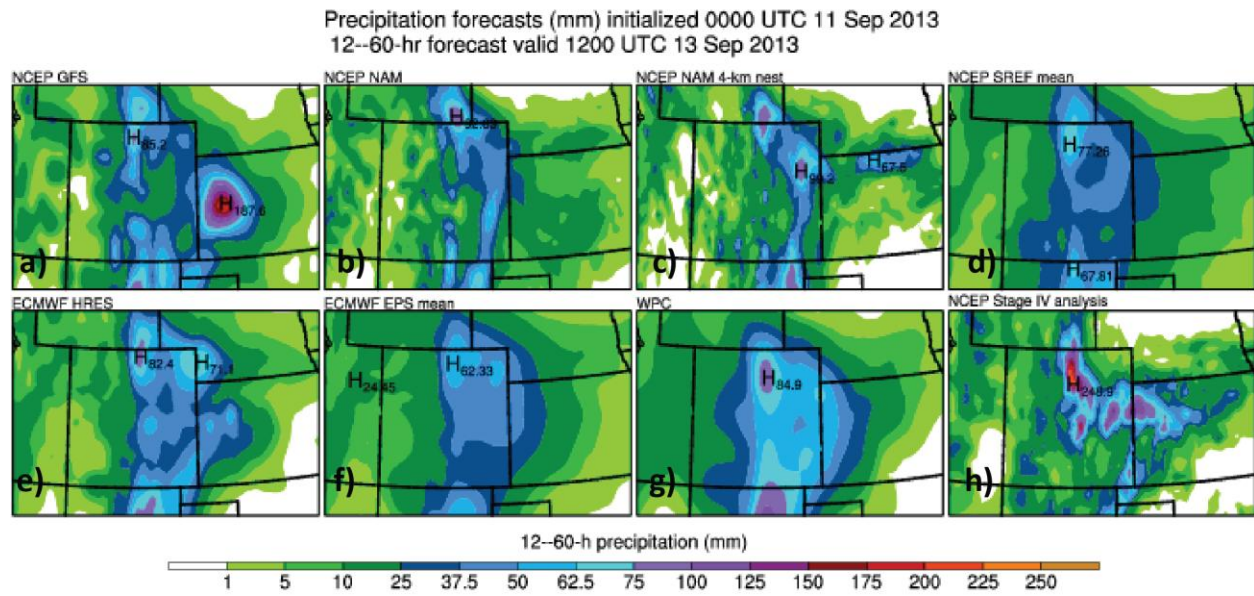
1111

1112

1113 **Figure 12.** Point-station bias estimates of 2-day (00 UTC 11 through 00 UTC 13 September)  
1114 estimated rainfall from a) KFTG Default Z-R, (b) KFTG Tropical Z-R, (c) KFTG Dual-pol based  
1115 esimates, (d) MPE, and (e) Stage IV. The bias is computed from QPE minus observation.

1116

1117

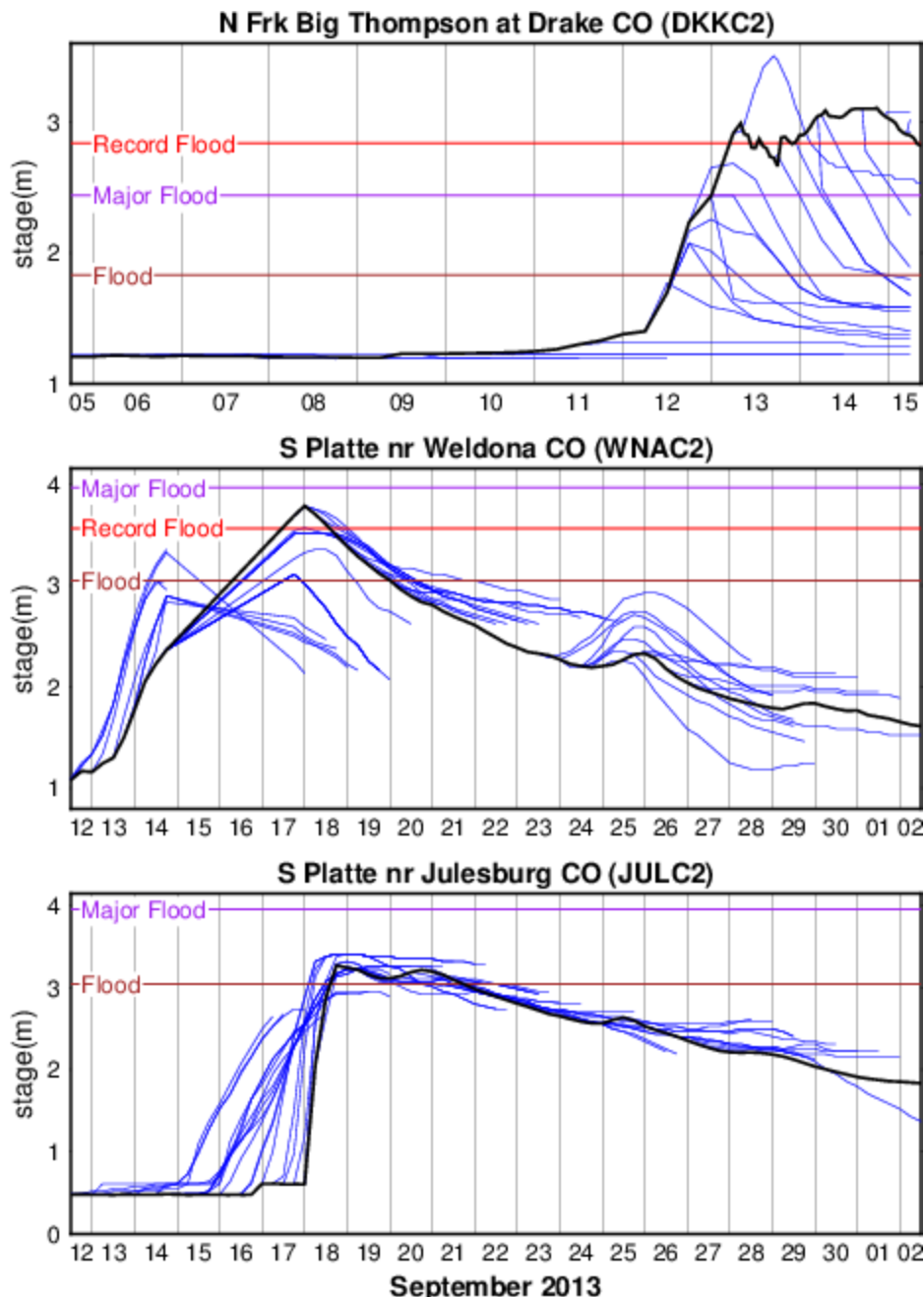


1118

1119

1120 **Figure 13.** Predicted and analyzed accumulated precipitation in the 48 hour period initialized  
1121 from 0000 UTC 11 September from a) NCEP Global Forecast System (GFS), b) NCEP North  
1122 American Model (NAM-12km), c) NCEP North American Model (NAM-4km), d) NCEP Short  
1123 Range Ensemble Forecast (SREF) mean, e) ECMWF High Resolution (HRES) model, f) ECMWF  
1124 Ensemble Prediction System (EPS) mean, g) NOAA Weather Prediction Center (WPC-human  
1125 forecast) and h) NCEP Stage IV merged radar-gauge analysis. All forecasts and the analysis were  
1126 regressed to a common 0.2° latitude/longitude grid.

1127



1128

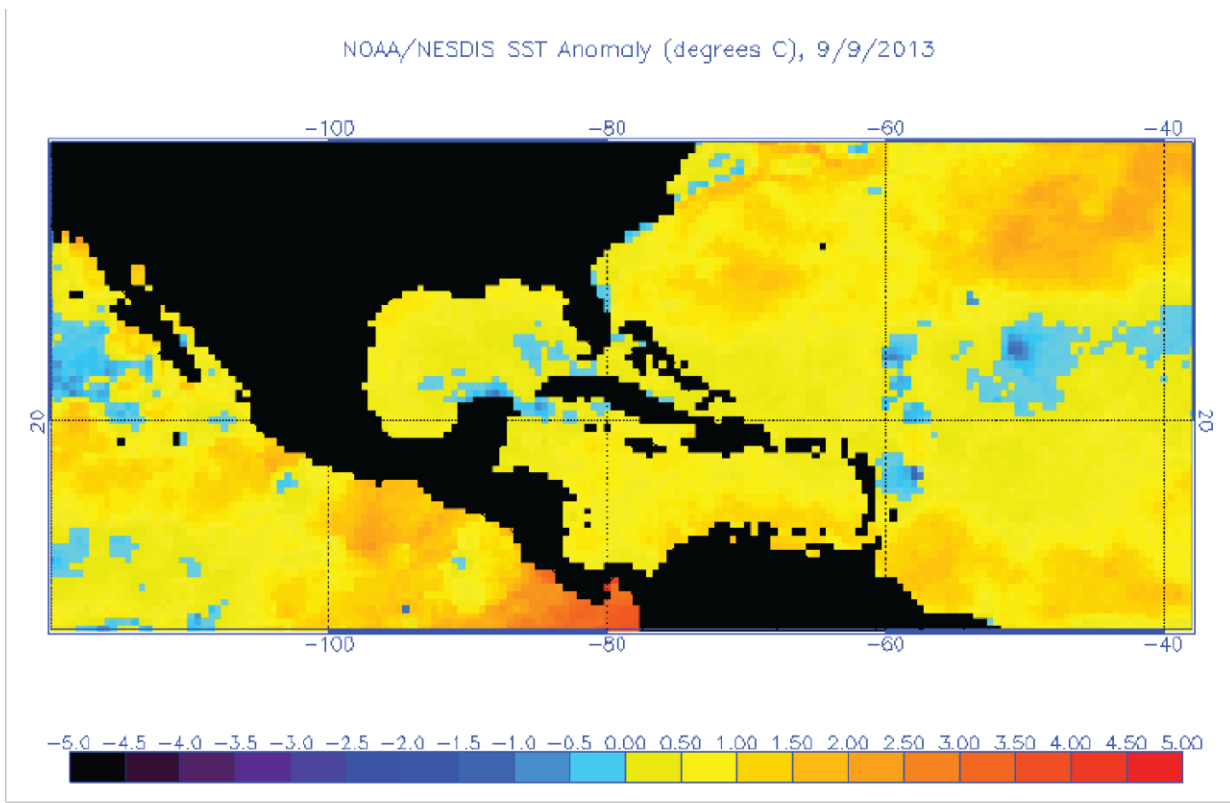
1129 **Figure 14.** NWS river stage forecasts (blue) and observations (black) for river locations with different  
1130 relative response times: fast (top), medium (middle), slow (bottom).

1131 **Appendices consist of four figures and a table, each called out in text as a separate Appendix**

1132

1133

1134

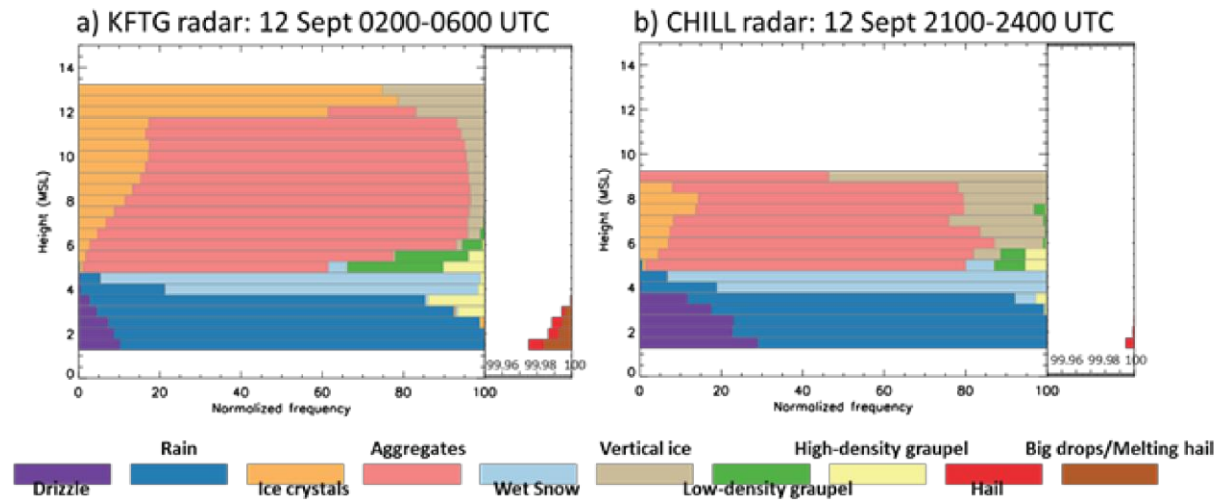


1135

1136 **Figure A1:** Sea-surface temperature anomaly (deg C) for 9 Sep 2013. (Source: NOAA/NESDIS)

1137

1138



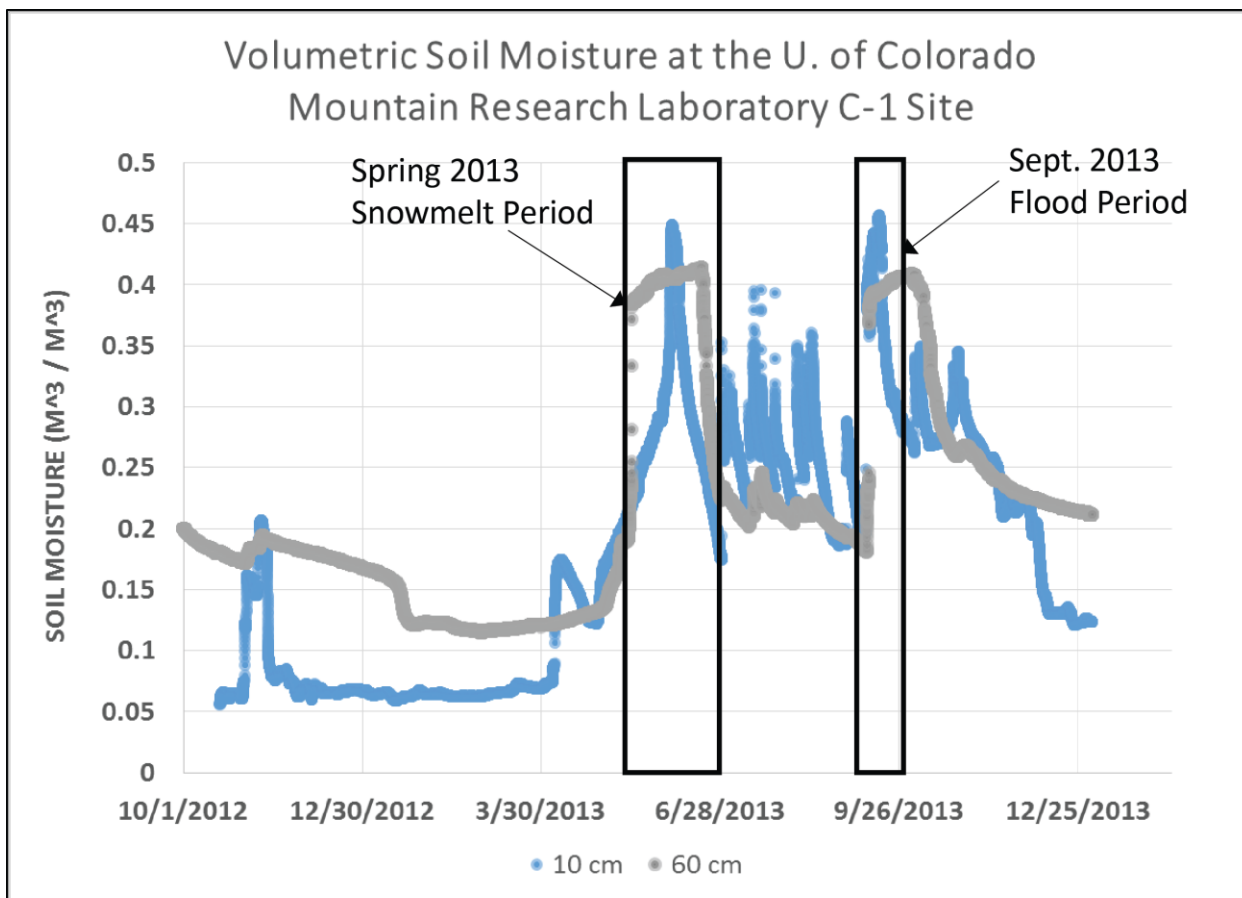
1139

1140

1141 **Figure A2:** Normalized frequency of occurrence of hydrometeor classification by height (km) for the time  
1142 period a) 02-05 Z using KFTG data and b) 21-24 UTC using CSU CHILL data. Big drops / melting hail and  
1143 hail have frequencies smaller than 0.05% and are therefore shown in the subset axes to the right of each  
1144 figure. [Although the same algorithm was used during both time periods, the polarized NEXRAD KFTG  
1145 radar was used during the early period (02-05 UTC) due to lack of corresponding CSU CHILL data. The  
1146 two radars have different scanning strategies, with the CSU CHILL radar performing fewer high elevation  
1147 angles to capture the upper levels. The plots are gridded to the same horizontal domain centered on  
1148 CHILL and facing west, with a 0.5 km horizontal and vertical resolution.]

1149

1150



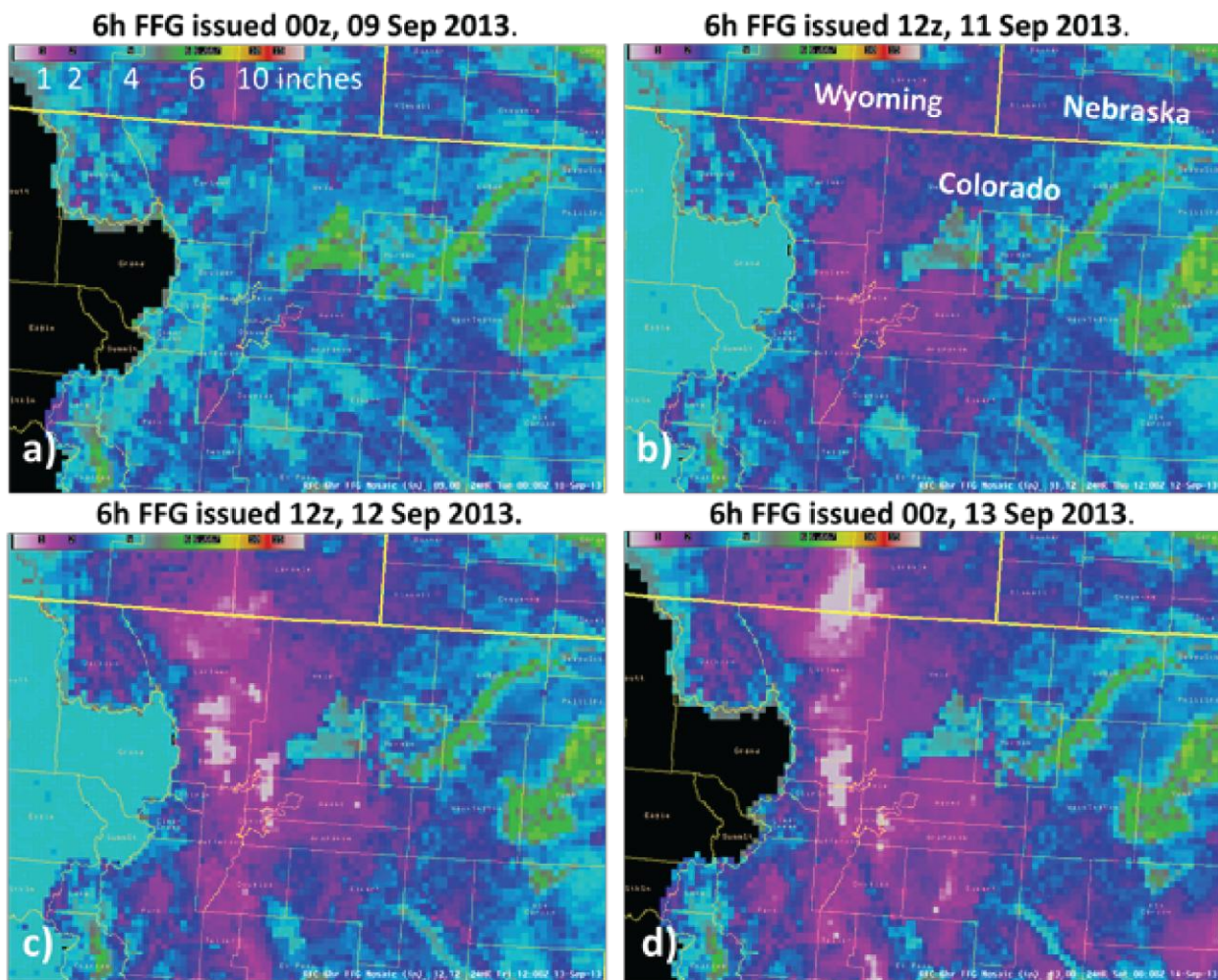
1151

1152

1153 **Figure A3.** Soil moisture values at 10cm and 60 cm depth from the U. of Colorado Mountain Research  
1154 Station at 3,300 m MSL elevation. The period from 1 October 2012 through 1 January 2014 is shown to  
1155 illustrate that values observed during the September 2013 floods were similar to saturated soil moisture  
1156 conditions observed during peak snowmelt periods.

1157

1158



1159

1160

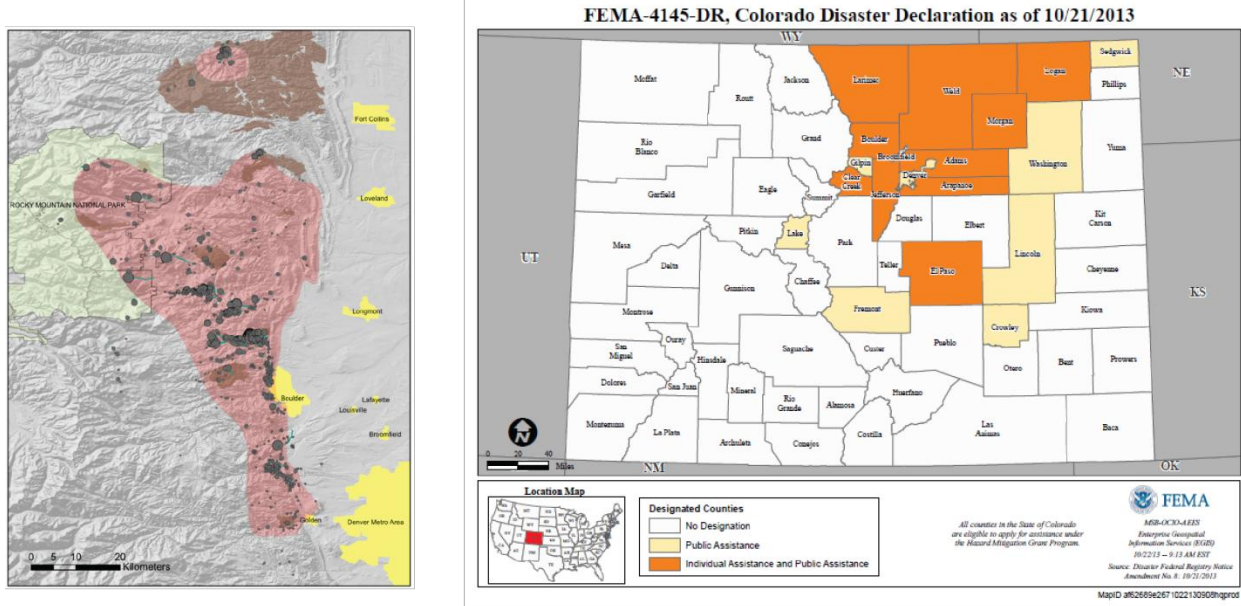
1161 **Figure A4.** Flash Flood Guidance (FFG) from Upper Missouri River Basin Forecast Center (MBRFC) for  
1162 four different forecast times from 9-13 September, 2013. Color shading indicates the threshold amount  
1163 of rainfall (inches) required to generate significant flooding.

1164

1165 **Figures in Sidebars:**

1166

1167



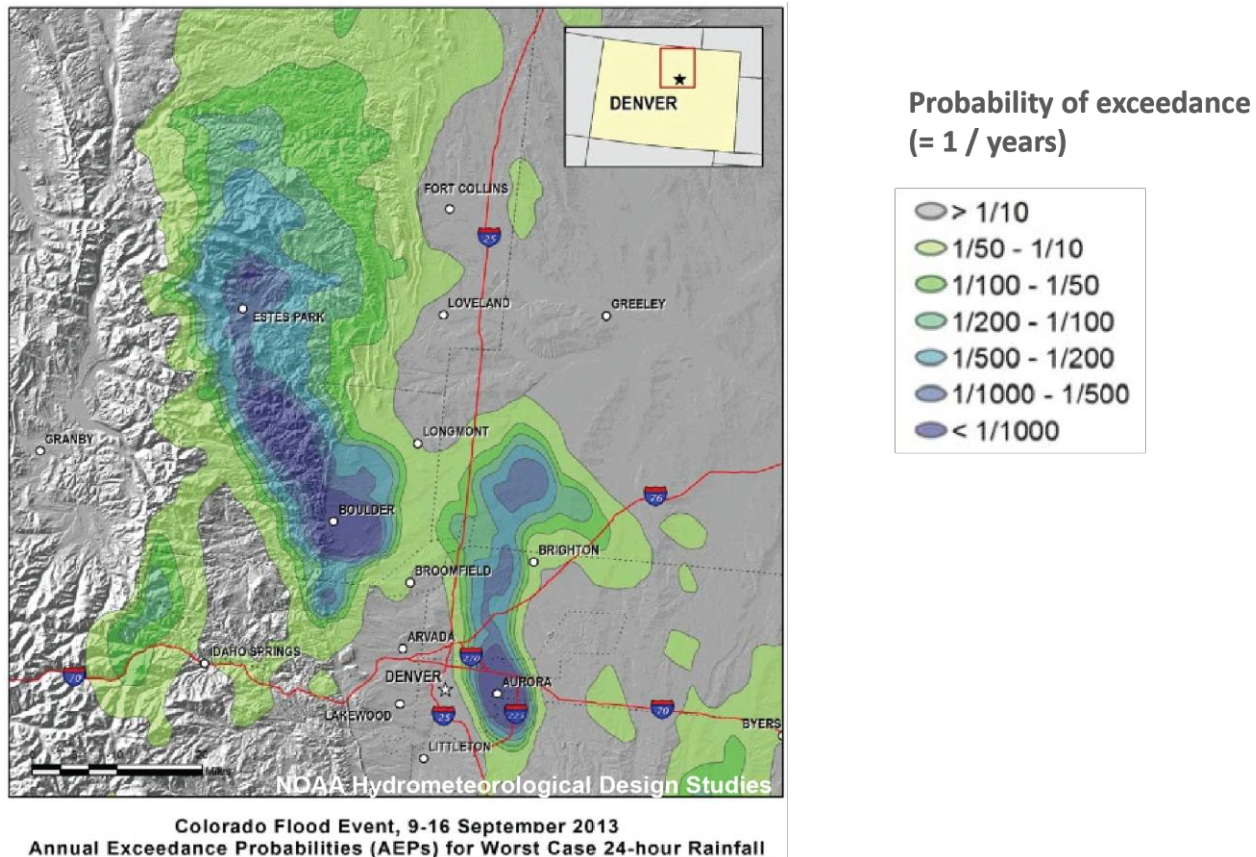
1168

1169

1170 **Figure SB1.** Map of over 1,100 documented hillslope failures by Jonathan Godt and Geff Coe of USGS.  
1171 Green dots are location and proportional size of hillslope failures, yellow shading denotes city areas, red  
1172 shading outlines region of heave rainfall, brown shading outlines regions of recent wildland fires, b)  
1173 FEMA Map of Colorado Disaster county declarations.

1174

1175



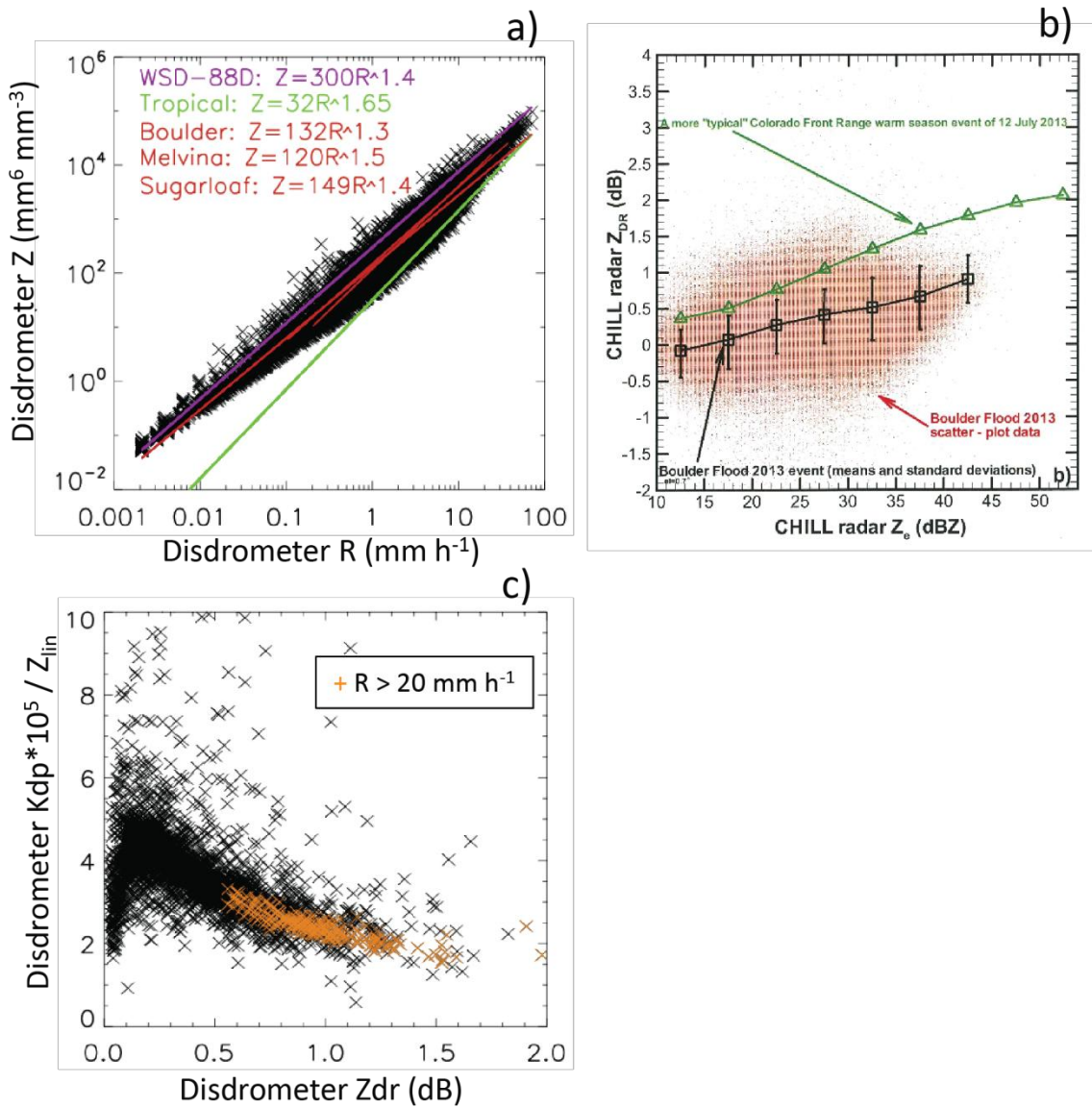
1176

1177

1178 **Figure SB2.** 9-16 September Annual Exceedance Probabilities for worst case 24-hour rainfall. (NWS  
1179 2013).

1180

1181



1182

1183 **Figure SB3.** Scatterplots showing ratios of a) disdrometer-based Z-R, and b) Zdr-Z relationship based on  
 1184 CHILL radar observations, c) disdrometer-based Kdp/Z-Zdr relationship. Disdrometer data is based on  
 1185 period shown in Fig. 6 (30 hours). CSU-CHILL radar data were analyzed between 1550 UTC 12 Sep until  
 1186 0240 UTC 13 Sep. a) and c) data are based on measurements at Boulder, Melvina Hill, and Sugarloaf.  
 1187 Red, green, and purple lines in a) represent Z-R relationships for the flood event based on three  
 1188 disdrometers, tropical rainfall, and non-tropical convective precipitation used by the WSD-88D radar,  
 1189 respectively. b) Green and black line represent typical mean values for a typical warm season rain event  
 1190 in the Front Range and for the Sept. 2013 flood event. Orange 'X's' in c) represent times when rainfall  
 1191 exceeded  $20 \text{ mm h}^{-1}$ .

1192